COMPUTATIONAL MODELING OF LASER-INDUCED DELAMINATION TESTING OF THIN FILMS

BY

PREMSAINATH COIMBATORE SELVARASU

THESIS

Submitted in partial fulfillment of the requirements
for the degree of Master of Science in Aerospace Engineering
in the Graduate College of the
University of Illinois at Urbana-Champaign, 2011

Urbana, Illinois

Adviser:

Professor Philippe H. Geubelle

Abstract

Thin film adhesion often determines microelectronic device reliability and it is therefore essential to have experimental techniques that accurately and efficiently characterize it. Laser-induced delamination is a novel technique that uses laser-generated stress waves to load thin films at high strain rates and extract the fracture toughness of the film/substrate interface. The effectiveness of the technique in measuring the interface properties of metallic films has been documented in previous studies. The objective of the current effort is to model the effect of residual stresses on the dynamic delamination of thin films. Residual stresses can be high enough to affect the crack advance and the mode mixity of the delimitation event, and must therefore be adequately modeled to make accurate and repeatable predictions of fracture toughness. The equivalent axial force and bending moment generated by the residual stresses are included in a dynamic, nonlinear finite element model of the delaminating film, and the impact of residual stresses on the final extent of the interfacial crack, the relative contribution of shear failure, and the deformed shape of the delaminated film is studied in detail. Another objective of the study is to develop techniques to address issues related to the testing of polymeric films. These type of films adhere well to silicon and the resulting crack advance is often much smaller than for metallic films, making the extraction of the interface fracture toughness more difficult. The use of an inertial layer which enhances the amount of kinetic energy trapped in the film and thus the crack advance is examined. It is determined that the inertial layer does improve the crack advance, although in a relatively limited fashion. The high interface toughness of polymer films often causes the film to fail cohesively when the crack front leaves the weakly bonded region and enters the strong interface. The use of a tapered pre-crack region that provides a more gradual transition to the strong interface is examined. The tapered triangular pre-crack geometry is found to be effective in reducing the stresses induced thereby making it an attractive option. We conclude by studying the impact of modifying the pre-crack geometry to enable the testing of multiple polymer films.

To my family for their unwavering support and patience

Acknowledgments

I am indebted to my adviser, Philippe H. Geubelle, for his constant guidance and support throughout my Masters degree, and for making it a wonderful experience. Without his patience and encouragement this work would not have been possible. I am extremely grateful to Prof. Nancy R. Sottos, for co-advising me and for her guidance especially in the experimental aspects of the project.

This work would not have been possible without the aid of several people and organizations. I am grateful for the support provided by the National Science Foundation under grant CMMI 0726742 and the Semiconductor Research Corporation under grant SRC 2008 KJ1773. Without the financial support provided by these organizations, this work would not have been possible.

I would also like to acknowledge my fellow colleagues in the Thin Film group - Phuong Tran, Martha Grady, Sharlottle Kramer and Ryan Van Echo for collaborating with me. Special thanks go to Phuong Tran for patiently explaining to me his thesis work and on whose efforts the current work is built on.

Many thanks to my colleagues Mohan Kulkarni, Alejandro Aragon, Fernando Stump, Soheil Soghrati, Kyle Smith, Christopher Ostoich, Mahesh Sucheedran, Scot Breitenfeld, Bharath Swaminathan, Mohith Manjunath and Amnaya Awasthi for the countless debates and fruitful exchange of ideas I have had with them over these two years.

I am also grateful to my family and friends for being a constant source of joy and affection in my life.plaining to me his thesis work and on whose efforts

Table of Contents

List of Tables vii

List of Figures viii

Chapter 1 : Introduction 1
1.1 Laser-Induced Spallation Testing 3
1.2 Objectives of the Study 5
1.3 Overview of the Dissertation 6

Chapter 2 : Numerical Model 7
2.1 Nonlinear Beam Element Model 7
2.2 Formulation 9
2.3 Implementation 12
2.4 Initial Load Calculation 12
2.5 Numerical Validation 14

Chapter 3 : Residual Stresses 17
3.1 Modeling and Implementation 18
3.2 Verification 19
3.3 Numerical Results 22

Chapter 4 : Dynamic Delamination of Polymer Films 30
4.1 Challenges Associated with Laser-Induced Testing of Polymer Films 30
4.2 Inertial Layer 32
4.3 Parametric Study 42
4.4 Pre-crack Geometry Modifications 45

Chapter 5 : Conclusions 54

Chapter A : Nonlinear Beam Element Formulation 56

Chapter B : Residual Stress Formulation 59

References 61

Author's Biography 65

List of Tables

3.1 Material properties used in the simulations. 22

4.1 Material property comparison of Al & PI. 32
4.2 Material property comparison of candidate materials for the inertial layer. . 38

List of Figures

1.1 Image of a multi-layered device and device failure by decohesion 1
1.2 Schematic of several adhesion test methods 2
1.3 Schematic of the laser-induced delamination test 3
1.4 Dynamic delamination experiment for toughness predictions 4

2.1 Schematic of the numeric model used 9
2.2 Exponential traction-separation law used 11
2.3 Kinetic energy envelope for a pre-crack 13
2.4 Energy evolution for an aluminum film with $6J/m^2$ as interface toughness . 14
2.5 Model validation - Crack advance 15
2.6 Model validation - Crack tip velocity 16

3.1 Picture of Aluminum film delamination 17
3.2 Schematic of Residual Stress Modeling 18
3.3 Static residual stress implementation verification test 20
3.4 Dynamic residual stress implementation verification test 21
3.5 Temporal profile of the laser-induced stress pulse 23
3.6 Mean stress effect on crack evolution 24
3.7 Mean stress crack advance comparisons 24
3.8 Mean stress effect on delamination shape 25
3.9 Mean stress effect on mode mixity 26
3.10 Stress gradient effect on crack evolution 27
3.11 Gradient stress crack evolution comparisons 28
3.12 Gradient stress effect on delamination shape 28
3.13 Gradient stress effect on mode mixity 29

4.1 Image of PI film test 31
4.2 Kinetic energy comparison for Al and PI 32
4.3 Schematic showing multi-layer beam scaling 33
4.4 Axial stress in a bi-material beam 35
4.5 Bending stress in a bi-material beam 36
4.6 Verification test for bi-material beam stress calculation 37
4.7 Kinetic energy comparison for candidate inertial layer materials 38

4.8 Crack advance comparison for different inertial layers 39
4.9 Crack advance and axial stress evolution in the initial load phase 40
4.10 Axial stress comparison for different inertial layers 41
4.11 Bending stress comparison for different inertial layers 41
4.12 Parametric study of axial stress and interface toughness 42
4.13 Parametric study of axial stress and interface toughness 43
4.14 Parametric study of bending stress and interface toughness 44
4.15 Crack advance comparison for various interface toughness values 44
4.16 Image of the triangular pre-crack 46
4.17 Crack advance comparison for triangular pre-cracks 46
4.18 Peak axial stress comparison for triangular pre-cracks 47
4.19 Bending stress comparison for triangular pre-cracks 48
4.20 Image of centered pre-crack geometry 49
4.21 Schematic of symmetric boundary conditions 49
4.22 Cohesive law with modifications for compressive regime as well 50
4.23 Delamination shape for edge and centered pre-crack 51
4.24 Crack advance comparison for edge and centered pre-crack 52
4.25 Mode mixity comparison between edge and centered pre-crack 52
4.26 Axial stress comparison between edge and centered pre-crack 53
4.27 Bending stress comparison between edge and centered pre-crack 53

Chapter 1

Introduction

Thin films form an essential part of most microelectronic devices used today and perform several key functions. Devices in use today are made up of multiple layers of different materials with vastly different material properties (Figure 1.1(a)). The length scale of the devices coupled with the widely varying material constituents results in several key reliability challenges [1]. Primary among them is interfacial decohesion caused by the thermo-mechanical loading generated during the operation of the device. The inherent stress concentration present at sharp edges of the device initiate an interface crack, which then propagates driven primarily by thermal loading (Figure 1.1(b)) [2, 3].

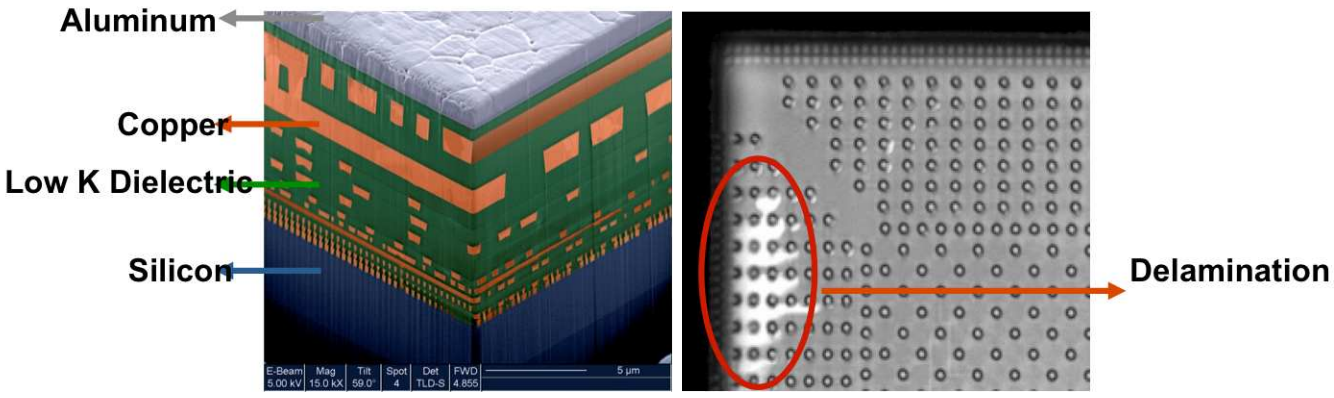

(a) (b)

Figure 1.1 – (a) Image of a 64 bit microprocessor showing the various layers made up of different materials. (b) Scanning acoustic microscope image depicting the decohesion failure of a microelectronic device. The delamination started at the edge of the film and propagated at the interface causing significant damage (*Taken from [4]*).

Thin film adhesion is a key parameter in determining the reliability of these devices and is characterized by two parameters, namely, the interface strength and the interface

toughness [5]. The interface strength is used as a measure of the crack initiation requirements. When the interface stress level exceeds a certain threshold value referred to as the interface strength, film decohesion occurs. Interface toughness on the other hand is a measure used to characterize crack propagation. This property is essential in order to design devices that resist fracture growth and operate without any interface decohesion issues.

Several techniques have been developed over the years to measure interface properties [6, 7, 8, 9]. A few of them are schematically depicted in Figure 1.2. Some of these techniques like the four-point bend test have been in use for years by the microelectronics industry and are quite popular. But these techniques suffer from some drawbacks, which make them unattractive for thin film adhesion characterization. A few of these techniques yield only a qualitative measure of the interface properties and as such cannot be used in any design process where quantitive inputs are required [9]. Others like the bulge test and the four-point bend test have the drawback of requiring elaborate specimen preparation, thereby reducing testing efficiency. But the key drawback associated with most of these testing methods is the large inelastic deformations associated with the loading technique [10]. The plastic deformation makes it difficult to estimate the actual amount of energy being dissipated at the fracture interface. Hence there is a need to design a new technique that addresses the shortcomings of the existing test methods.

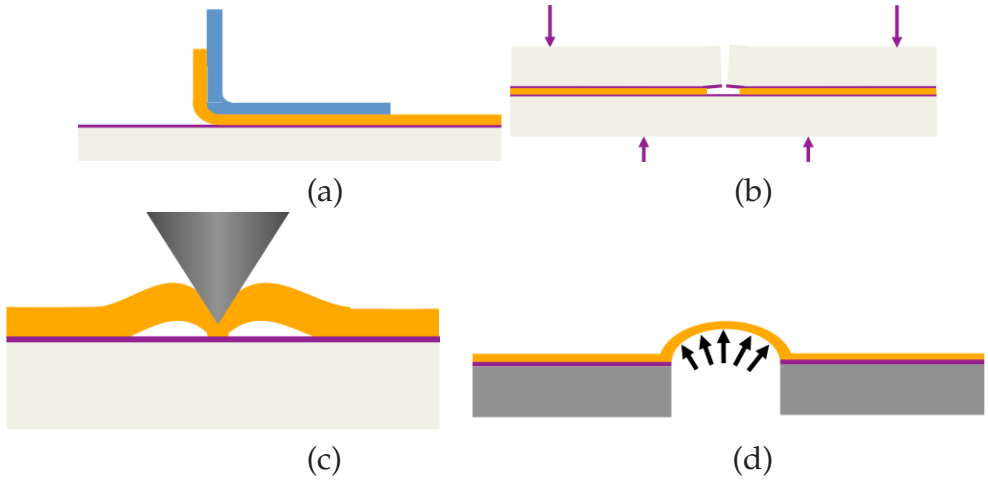

Figure 1.2 – Schematic of (a) Tape peel test where the film is pulled with the help of an adhesive tape. (b) Four-point bend test where the crack propagates at the interface due to the bending strain energy. (c) Nano-indentation test where the toughness is measured by the material pile-up around the tip. (d) Bulge test where the film is bulged out by the pressure acting on the inside of the film (*Taken from [11]*).

1.1 Laser-Induced Spallation Testing

Laser-induced spallation is an experimental technique used to determine interface properties by loading the interface dynamically using a laser pulse. Laser-induced delamination has several salient features which make it an attractive option over other test methods [12, 13, 14, 15, 16]. Primary among them is the precise, non-contacting manner through which the technique loads the interface using a laser pulse of very short duration (typically 10 to 15 *ns*) and high amplitude (hundreds of *MPa*). The very high loading rate enables the measurement of the interface characteristics with little plastic deformation [5], allowing for a more precise determination of the intrinsic interface properties.

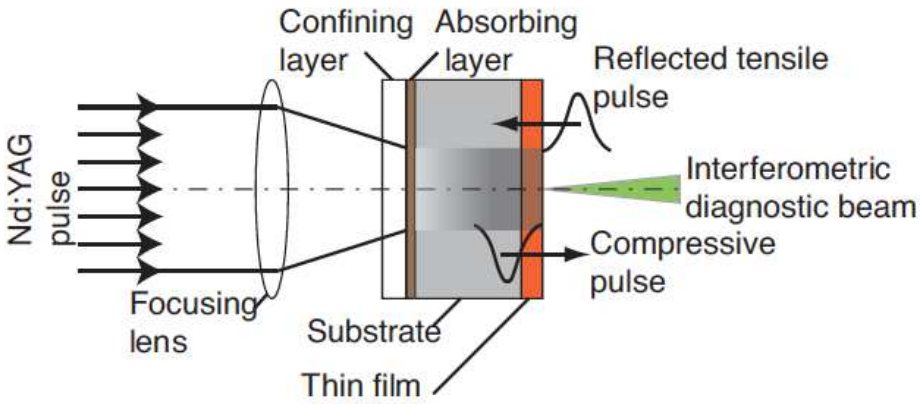

Figure 1.3 – Schematic of the laser-induced spallation test. The pulse generated by the ablation of the absorbing layer located on the back side of the substrate gets reflected back from the free surface of the film as a tensile wave and causes the failure of the film. The displacement of the film is measured using an interferometric diagnostic beam (*Taken from [11]*).

The laser pulse is focussed on a sacrificial ablation layer deposited on the back side of the substrate. The ablation generates a compressive stress wave that propagates through the substrate and across the interface, gets reflected at the free surface of the film as a tensile wave and loads the interface in tension causing delamination as depicted in Figure 1.3. The strain rates associated with the laser pulse loading are in the order of $10^7\ s^{-1}$, thereby ensuring that there is limited plastic deformation in the film. In the original form of the laser spallation test, the loading was primarily tensile in nature and provided a measure of the tensile interface strength. More recently, Wang et al. [17] and Kitey et al. [18]

have developed versions of the delamination experiment that uses mode conversion along inclined free surfaces and/or interfaces to induce mixed-mode loading of the film/substrate interface. This type of laser-induced tests, which are performed on blanket films, provide measurements of the interface strength of the film, which, as indicated earlier, is associated with crack initiation. To measure the interface toughness, which is needed for crack advance predictions, one needs to achieve a controlled delimitation event, preferably over large distances (several millimeters).

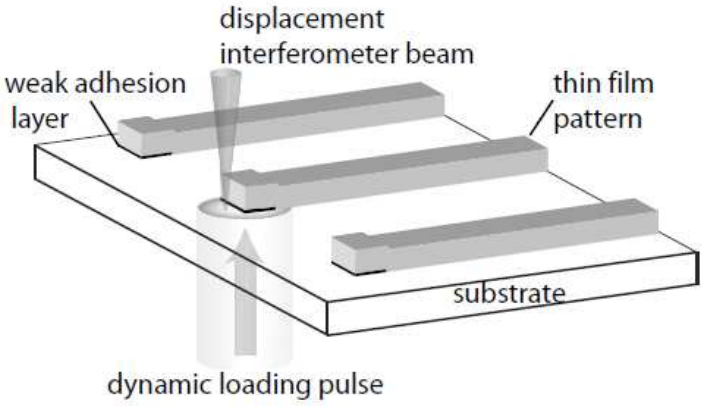

Figure 1.4 – Schematic of laser-induced delamination test. The test geometry includes a weak adhesion layer, which serves as pre-crack region and, when hit by the laser pulse, spalls instantly. The kinetic energy trapped in the pre-cracked region of the patterned film then gets converted into fracture energy as the film delaminates over several millimeters (*Taken from [4]*).

To that effect, Kandula et al. [5] have developed an experimental protocol to achieve a controlled delamination of a patterned thin film by using a weak adhesion region in the laser loading zone. The weak adhesion region behaves like a pre-crack, ensuring that the kinetic energy associated with the laser loading pulse is effectively channeled to the interface, resulting in crack propagation that may span several millimeters. The schematic of the delamination test is shown in Figure 1.4. The fracture toughness of the interface is then calculated using the assumption that most of the kinetic energy imparted to the pre-crack region is channeled into the fracture process. The final delaminated crack length is then used to estimate the fracture toughness (G_c) based on the simple energy balance relation

$$G_c = \frac{a_o K_{1D}}{a_f - a_o}, \tag{1.1}$$

where K_{1D} is the kinetic energy per unit area imparted to the pre-crack region and esti-

mated analytically or numerically using the 1D elastodynamics relations describing the propagation of the laser-induced wave through the film and back from the free surface, a_o is the initial pre-crack length, and a_f, the final crack length. Only a small fraction of the total energy goes into straining the delaminated film, while most of the kinetic energy is channeled into the failure process. The extent to which the kinetic energy is channeled to the fracture process is affected by various parameters including the film geometry, load pulse characteristics, etc. Tran et al. [19] performed extensive parametric studies to characterize the mechanics of the delamination process and to check the validity of energy balance assumption.

1.2 Objectives of the Study

The primary objective of the modeling effort described in this document is to develop computational models that enable the study of the dynamic delimitation event. Tran et al. [19] have developed a physically accurate and computationally efficient numerical model based on non-linear beam and cohesive elements. The numerical model has been used to establish the validity of the energy balance assumption and to perform a detailed parametric study concerning the impact of the specimen geometry, loading conditions and interface properties. The numerical model developed by Tran et al. is used as the basis of the modeling work described hereafter and is extended to include the effect of residual stresses in the film. Residual stresses can be a very significant factor in thin films and one of the primary objectives of the current work is to model the impact residual stresses have on the thin film delamination failure. Another key objective of the present study is to support the extension of the laser-induced delamination technique to other, more complex material systems like polymer films. The previous studies utilized metallic films that have vastly different material properties (stiffness, density, ...) than polymer films. Polymer films in general are much lighter and therefore do not allow storing as much kinetic energy as their metallic counterparts. Polymeric films also have better adhesion to silicon substrates, which limits the extent of crack advance, and thereby renders the extraction of the fracture toughness more difficult. This work aims to support the development of the necessary modifications to the testing technique to enable the successful laser-induced testing of polymer films.

1.3 Overview of the Dissertation

The second chapter discusses in detail the numerical model developed by Tran et al. [19] as it forms the basis of the current work. The rationale for choosing a numerical model based on nonlinear beam elements and cohesive finite elements is discussed. Then we review the formulation and implementation adopted for the nonlinear beam and cohesive elements, and we describe how the initial conditions of the simulations are obtained using the output of a 1D elastodynamic code. Finally we present the validation study performed by Tran and co-workers based on direct measurements of the evolution of the crack advance in a metallic film.

In Chapter 3, we discuss in detail the impact of residual stresses on the delamination mechanics. The chapter begins with a discussion of the modeling of residual stresses and how the arbitrary variation of residual stresses across the thickness is decomposed. This is followed by a detailed description of the modifications introduced in the dynamic, implicit finite element solver to model residual stresses. Static and dynamic verification studies are then presented, followed by the results of the actual study of the impact of residual stress distributions on the dynamic delamination process. Special emphasis is placed on the effect of the resultant residual axial force and bending moment on crack extent, delaminating film shape and failure mode mixity.

The fourth chapter focusses on the numerical efforts aimed at enabling polymer film testing. The impact of adding an inertial layer to enhance crack advance of the film is first investigated. The addition of the inertial layer requires modifications to the numerical model and to the axial stress calculation as the film becomes a multi-layered stack. The impact of the inertial layer on crack advance and the amplitude of the axial stresses induced during the initial loading phase is examined. A parametric study examining the variation of film stress with the interface toughness is then presented. We then explore the option of using a triangular shape for the pre-crack in order to avoid the observed cohesive failure of the film when the crack reaches the strong interface. Finally we summarize a study aimed at quantifying the impact of changing the pre-crack geometry to improve the efficiency of the test.

Chapter 2

Numerical Model

In this chapter, we summarize the basic formulation and implementation of the numerical model developed by Tran et al. [19], which serves as the basis of the current study. The model is based on an implicit, dynamic, nonlinear finite element solver that combines nonlinear beam elements to model the response of the film, and cohesive elements used to capture the initiation, propagation and arrest of the delimitation front. The numerical scheme has been found by Tran and co-workers to be computationally efficient and physically accurate. In the first part of the chapter, the rationale behind the numerical model is presented, followed by a summary of the formulation. We then describe some of the details of the numerical implementation of the model, including the method used to calculate the initial conditions associated with the arrival of the laser pulse. Finally, in the interest of completeness, we reproduce the validation study first presented by Tran and co-workers and based on direct measurements of the dynamic delamination event performed by Kandula et al.

2.1 Nonlinear Beam Element Model

The failure or decohesion along bi-material interfaces has been extensively studied in the past using a variety of analytical techniques. Suo and Hutchinson [20] provided the complete solution to the case of a semi-infinite crack lying along the interface of two elastic layers subjected to general loads. Hutchinson [21] studied extensively the mixed-mode behavior of interface cracks due to the asymmetry in loading and elastic properties across the interface. Hu et al. [22] studied the decohesion of films from brittle substrates using metallic films on glass substrates. They found that the crack extends into the substrate and acquires a steady-state trajectory parallel to the substrate. Thouless and Jensen [23]

studied the impact of residual stresses on blister tests and obtained analytical solutions for the additional energy released upon the relaxation of these stresses.

Over the years, numerical models of varying complexity and different levels of detail have been used to study dynamic delamination of thin films. In general, for the problem of interest, the numerical model should have the capability to capture the dynamic response of the film as it delaminates, and the fracture processes occurring at the film-substrate interface must be accounted for by suitable means. Several approaches exist to model the damage occurring due to fracture and material decohesion. Cohesive zone modeling approach, pioneered by Dugdale [24], Barrenblatt [25], Rice [26] and others, considers fracture to be a phenomena where separation occur over a small region located ahead of the crack tip and referred to as the cohesive zone. Cohesive zone modeling, and its finite element implementation referred to as cohesive elements, have been used to represent a wide range of failure processes in thin films and multi-layer systems, such as microcracking and decohesion of films under tension [27], decohesion of thin film segments [28], laser-induced blistering [29] and delamination of weakly bonded coatings in indentation tests [30].

Laser-induced delamination has also been modeled using several techniques. Liang et al. [31] performed a transient finite element (FE) analysis that included a volumetric damage model to model the dynamic failure response of a blanket film/substrate system. Tran et al. [32] have used a 2D hybrid spectral/finite element scheme combined with a rate-independent extrinsic bilinear cohesive model [33] to simulate the delamination process. These FE and FE/spectral analyses provide extensive details on the dynamic failure process, but are computationally very expensive and are therefore not amenable to large parametric studies.

To reduce the computational effort, more simplified models have been developed, based primarily on a beam representation of the film. A number of problems involving thin films have been successfully modeled using nonlinear beams and cohesive elements [34], [19]. A nonlinear beam formulation is essential as the film undergoes large deformation and rotation when it delaminates from the substrate. The use of linear beam models leads to spurious loss of bending stiffness, which has been directly linked to the inability of the linear theory to account for the changes in bending stiffness due to axial loading (Simo et al. [35]). Furthermore, Tran et al. [32] found using the aforementioned spectral/FE method that very little energy is leaked back into the substrate during the delamination event and hence the substrate can be considered to be perfectly rigid. Therefore, only the film is modeled with nonlinear beam elements while cohesive elements are used to model the initiation, propagation and arrest of the delamination front. The simplified model,

schematically shown in Figure 2.1, can thus accurately model the physics of the problem.

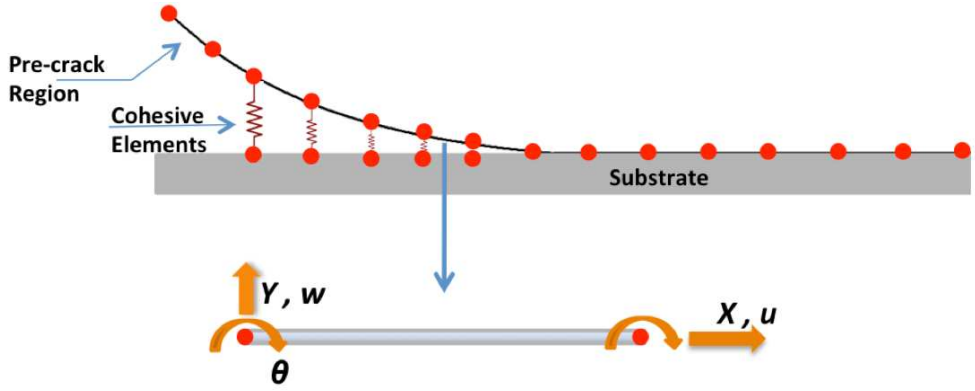

Figure 2.1 – Schematic of the numerical model used to simulate the dynamic delamination event, including details on the beam element.

2.2 Formulation

2.2.1 Nonlinear Beam Elements

To capture the large deformation effects, we have adopted the von Karman nonlinear beam theory, for which the axial strain is defined as [19]

$$\epsilon_x = \frac{\partial u}{\partial x} + \frac{1}{2}\left(\frac{\partial w}{\partial x}\right)^2, \tag{2.1}$$

where w denotes the transverse deflection of the beam, and u, the axial displacement, which is obtained by the superposition of the axial stretching and bending components:

$$u = u_0 - \eta\frac{h}{2}\frac{\partial w}{\partial x}. \tag{2.2}$$

Here, u_0 refers to the axial displacement along the neutral axis, h is the beam thickness, and the parameter η takes a value between $[-1, +1]$ and represents the position along the thickness direction. The axial strain can then be expressed as [19]

$$\epsilon_x = \frac{\partial u_0}{\partial x} + \frac{1}{2}\left(\frac{\partial w}{\partial x}\right)^2 - \eta\frac{h}{2}\frac{\partial^2 w}{\partial x^2}. \tag{2.3}$$

Assuming a linearly elastic response of the beam, the axial stress is given by

$$\sigma_x = \tilde{E}\epsilon_x, \tag{2.4}$$

where $\tilde{E} = E/(1-\nu^2)$, with E and ν denoting the Youngs modulus and Poissons ratio, respectively. This stems from the plane strain assumption used for the beam as the film thickness is small in comparison with the film width in the out-of-plane direction.

2.2.2 Cohesive Elements

As described earlier, the fracture process occurring at the interface is represented using cohesive elements. Like many cohesive laws available in the literature, the cohesive model is based on a cohesive potential, the gradients of which yields the cohesive tractions acting along the cohesive zone. The potential adopted in the present study is denoted by ψ and represents the cohesive free energy density per unit area. The traction $\boldsymbol{t_0}$ is defined as [36].

$$\boldsymbol{t_0} = \frac{\partial \psi}{\partial \boldsymbol{\delta}} = \frac{\hat{t}}{\hat{\delta}}\boldsymbol{t}, \tag{2.5}$$

$$\boldsymbol{t} = [\beta^2 \boldsymbol{\delta} + (1-\beta^2)(\boldsymbol{\delta}\cdot\boldsymbol{N_c})\boldsymbol{N_c}], \tag{2.6}$$

where $\boldsymbol{\delta}$ denotes the displacement jump vector, $\hat{\delta}$ the effective displacement jump and $\hat{t}$ the effective traction vector. The parameter $\beta \in [0,1]$ is referred to as the mode mixity factor, while $\boldsymbol{N_c}$ represents the unit normal to the cohesive surface. The mode mixity parameter assigns different weights to the sliding and normal opening displacements to simulate mixed-mode failure. The effective displacement jump and traction are given by [36]

$$\hat{\delta} = \sqrt{\beta^2 \hat{\delta}_s^2 + \hat{\delta}_n^2}, \tag{2.7}$$

$$\hat{t} = \frac{\partial \psi}{\partial \hat{\delta}}, \tag{2.8}$$

where $\hat{\delta}_s$ and $\hat{\delta}_n$ represent the sliding and normal displacement jumps, respectively, and are defined as

$$\hat{\delta}_s = |\boldsymbol{\delta_s}|, \tag{2.9}$$

$$\boldsymbol{\delta_s} = (1 - \boldsymbol{N_c}\otimes\boldsymbol{N_c})\boldsymbol{\delta}, \tag{2.10}$$

$$\hat{\delta}_n = \boldsymbol{\delta} \cdot \boldsymbol{N_c}. \tag{2.11}$$

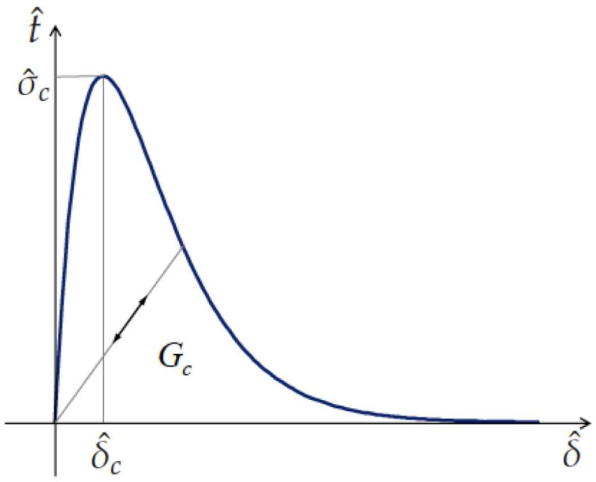

Figure 2.2 – Exponential traction-separation law with $\hat{\sigma}_c$ as the interface strength and $\hat{\delta}_c$ the corresponding critical opening displacement. The dotted line to the origin denotes an unloading and reloading path during partial failure (*Taken from [36]*).

In this study, the mathematically convenient rate-independent exponential model (Figure 2.2) proposed by Ortiz and Pandolfi [37] is used for the traction-separation law. The potential function ψ takes the exponential form [36]

$$\psi = e\hat{\sigma}_c\hat{\delta}_c\left[1 - \left(1 + \frac{\hat{\delta}}{\hat{\delta}_c}\right)exp\left(\frac{-\hat{\delta}}{\hat{\delta}_c}\right)\right], \tag{2.12}$$

$$\hat{t} = \frac{\partial\psi}{\partial\hat{\delta}} = e\hat{\sigma}_c\frac{\hat{\delta}}{\hat{\delta}_c}exp\left(\frac{-\hat{\delta}}{\hat{\delta}_c}\right), \tag{2.13}$$

where $e = \exp(1)$, $\hat{\sigma}_c$ denotes the maximum effective cohesive traction, and $\hat{\delta}_c$ is the critical effective opening displacement jump beyond which the interface experiences damage. The cohesive fracture energy dissipated is represented by the area under the traction-separation law and is given by

$$G_c = \int_0^\infty \hat{t}d\hat{\delta} = e\hat{\sigma}_c\hat{\delta}_c. \tag{2.14}$$

2.3 Implementation

The film is discretized using two-noded nonlinear beam elements, with each node having three degrees of freedom: axial and transverse displacements, and rotation. Linear interpolation is used for the axial degree of freedom while the classical hermitian shape functions are used for the transverse and rotational degrees of freedom. A co-rotational framework is adopted to account for the large rotations experienced by the film as it delaminates [38]. This approach uses a local element reference system which rotates with the element as it undergoes large rotations to account for the rigid body motions.

The principle of virtual work for this problem takes the form

$$\int_0^L \rho A \frac{\partial^2 \mathbf{u}}{\partial t^2}.\delta\mathbf{u}\, dx + \int_0^L (\sigma\delta\varepsilon)A\, dx = \int_0^L \mathbf{T}.\delta\mathbf{\Delta}\, dx + \int_0^L \mathbf{T_{ex}}.\delta\mathbf{u}\, dx, \tag{2.15}$$

where L the length of the beam, ρ is the material density, A the cross-sectional area of the beam, $\mathbf{u}$ the displacement vector, t denotes time, σ the stress, $\delta\varepsilon$ the variation of strain, $\mathbf{T}$ the cohesive traction force, $\delta\mathbf{\Delta}$ the variation of the displacement jump across the film/substrate interface, $\mathbf{T_{ex}}$ the external traction force and $\delta\mathbf{u}$ the variation of displacement. The internal force vector is obtained by taking the first variational derivative, while the second variational derivative yields the tangent stiffness matrix. Both the internal force vector and the tangent stiffness matrix are derived in Appendix A. The resulting semi-discrete equation is

$$M\frac{\partial^2 U}{\partial t^2} + R_{in}(U) = R_{coh}(U) + R_{ext}, \tag{2.16}$$

where M is the mass matrix, U represents the nodal displacement vector while R_{in} ,R_{coh} and R_{ext} are the internal, cohesive and external force vectors, respectively. The semi-discrete equation is time discretized using a predictor-multicorrector Newmark scheme [39] and the system of nonlinear equations is solved iteratively at every time step using the Newton-Raphson scheme. In an effort to reduce the computational costs further, several speed-up techniques have been implemented, including spatial and temporal adaptivity. Tran et al. [11] indicate that the adaptive nonlinear beam model provides a three order of magnitude speed-up compared to the hybrid spectral/FE scheme.

2.4 Initial Load Calculation

In the experiment, the sacrificial layer located below the pre-crack region is hit with a laser pulse of certain fluence which determines the strength of the stress pulse produced. Due

to the confinement created by the waterglass layer, a compressive stress wave is generated and travels through the substrate and the film, gets reflected as a tensile wave from the free surface of the film and loads the interface in tension. The high tensile load causes the weak interface at the pre-crack to spall almost instantaneously. The energy imparted by the laser pulse is thus trapped in the form of kinetic energy in the pre-crack portion of the film. The initial laser pulse load is modeled in the form of an initial velocity applied to the nodes located in the pre-crack portion alone. The imparted kinetic energy is determined using an explicit 1D elastodynamic model for the propagation of the laser-induced stress wave through the layers and interfaces. The 1D model enables the calculation of the interface stress as well as the kinetic energy trapped in the film. The kinetic energy can be plotted against the interface stress to generate a kinetic energy envelope as shown in Figure 2.3, which has been obtained for the case of a 1.5 *GPa* substrate pulse of 10 *ns* duration propagating in a 1D fashion through a multilayer system composed of a Si substrate, an Au layer of 200 *nm* thickness, and a 4 μm-thick film of Al.

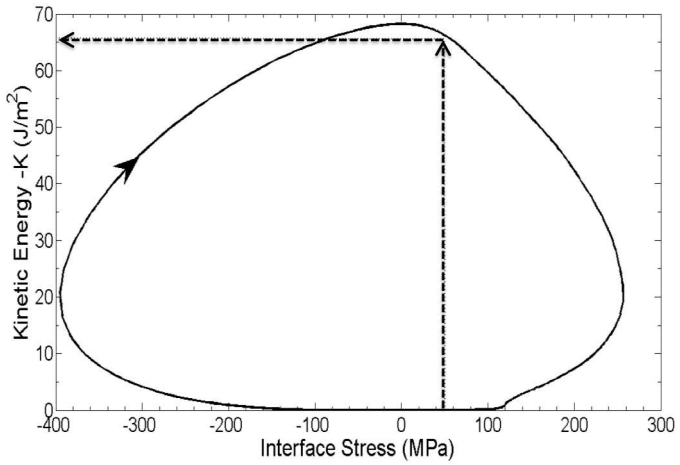

Figure 2.3 – Kinetic energy envelope obtained with an 1D elastodynamic code for the case of Si/Au/Al pre-crack system. The strength of the weak Au/Si interface is 50 *MPa*, which corresponds to a kinetic energy per unit area, K_{1D}, of 66 J/m^2 at the time of spallation of the portion of the film in the pre-crack region. The arrow associated with the solid curve denotes the evolution of the kinetic energy versus interface stress relation, as the interface stress is at first compressive at the arrival of the compressive pulse from the substrate, and then becomes tensile due to the reflection from the free surface of the film.

The weak interface between the gold and silicon has an interface strength of 50 *MPa* and, when the interface stress reaches that value, the spallation of the pre-crack region occurs. The corresponding kinetic energy is the kinetic energy per unit area trapped in the film as depicted in Figure 2.3. The kinetic energy calculated using the explicit 1D elastodynamic

code is designated by K_{1D}. The computed value of K_{1D} is then used to extract the initial vertical velocity V_0 imparted to the nodes located in the pre-crack region as

$$V_0 = \sqrt{\frac{2K_{1D}}{\rho_{film}h}}. \tag{2.17}$$

2.5 Numerical Validation

The numerical model has been validated by Tran and co-workers [11] by comparing its predictions to that of direct experimental observations of the crack advance during the dynamic delamination event. The specimen geometry, taken directly from the experimental set up, consists of a 4.3 μm thick Al layer and 330 μm long pre-crack region where a 200 nm thick Au weak adhesion layer is sandwiched between the film and the substrate. The adhesive strengths measured by Kandula [5] are 300 and 50 MPa for the Al/Si and Au/Si interfaces, respectively. The film is subjected to a 10 ns Gaussian-like pulse loading with an amplitude of 1.5 GPa. For such a system, the initial velocity V_0 calculated using the process detailed above was found to be 147 m/s. Assuming an interface toughness of

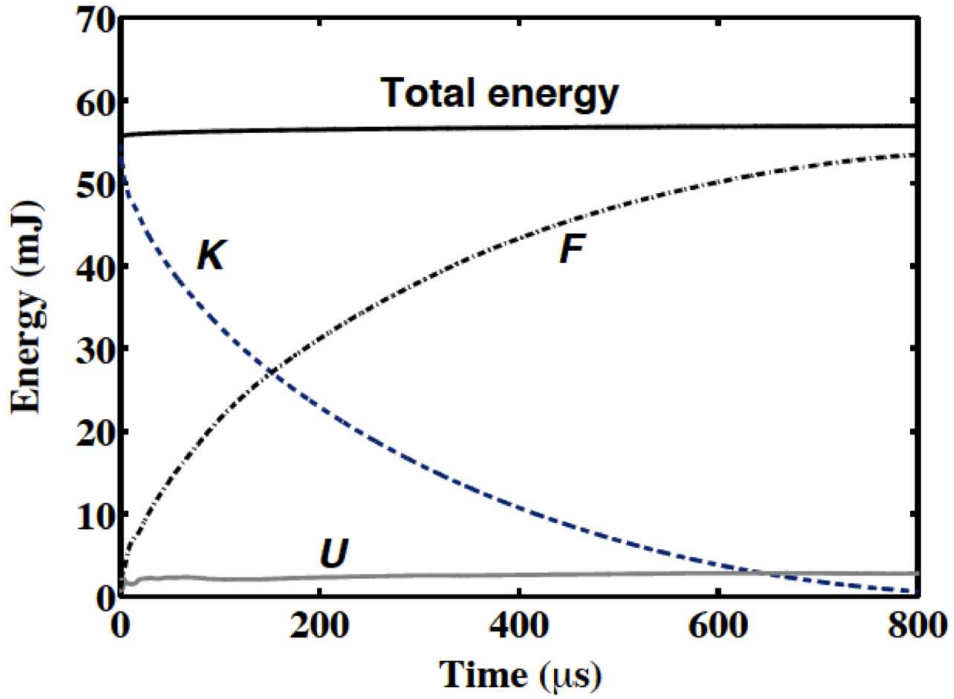

Figure 2.4 – Evolution of kinetic (K), fracture (F) and strain energy (U) energy components during the dynamic delamination event (*Taken from [11]*).

6 J/m^2 for the Si/Al interface, the dynamic nonlinear beam/cohesive FE model yields the evolution of the various components of energy shown in Figure 2.4. As the interface delamination progresses, the kinetic energy (denoted by K) imparted to the pre-crack region is gradually dissipated by the failure processes occurring at the interface, as apparent from the increasing fracture energy curve (denoted by F). The adopted cohesive model is rate independent and hence the evolution of fracture energy mirrors that of the crack advance. After approximately 800 μs, the kinetic energy available runs out and the delamination event ends. Throughout the delamination process, a portion of the energy is converted into strain energy (denoted by U). But that portion remains small, less than 5% of the total energy available in the system, validating the assumption behind the energy balance that led to Equation (1.1).

A comparison between numerical predictions and experimental measurements of the corresponding crack advance is presented in Figure 2.5. The numerical simulations were conducted with toughness values of 5 and 6 J/m^2 [19], which are similar to those measured using a quasi-static four-point bend test [40]. Very good agreement is observed with the experimental results, validating the numerical model. A similar agreement is obtained between numerical and experimental evolutions of the crack tip speed, as shown in Figure 2.6.

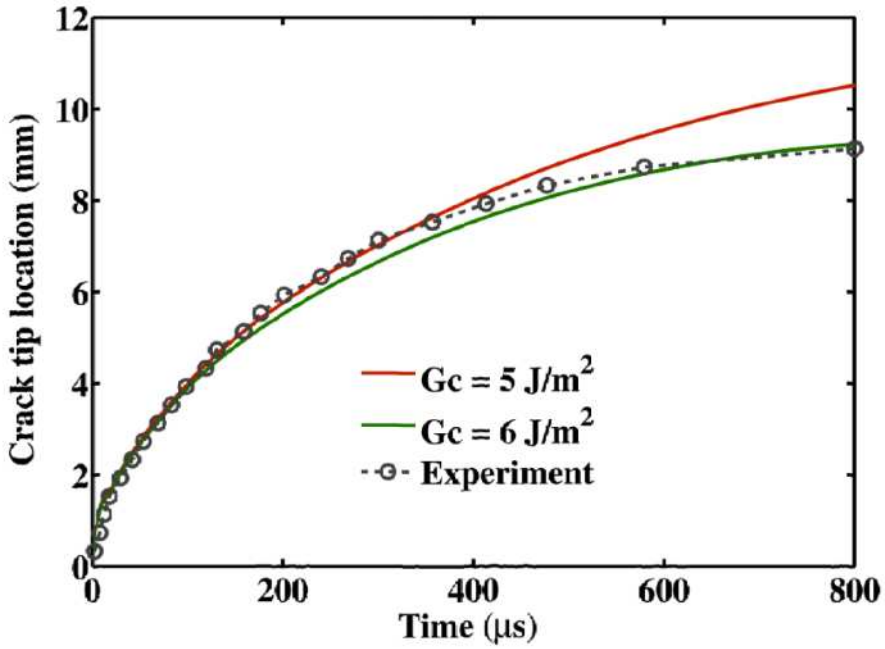

Figure 2.5 – Comparison of numerical crack advance predictions with the experimental data for a Si/Al system. The numerical results are obtained for two different interface toughness values (*Taken from [11]*).

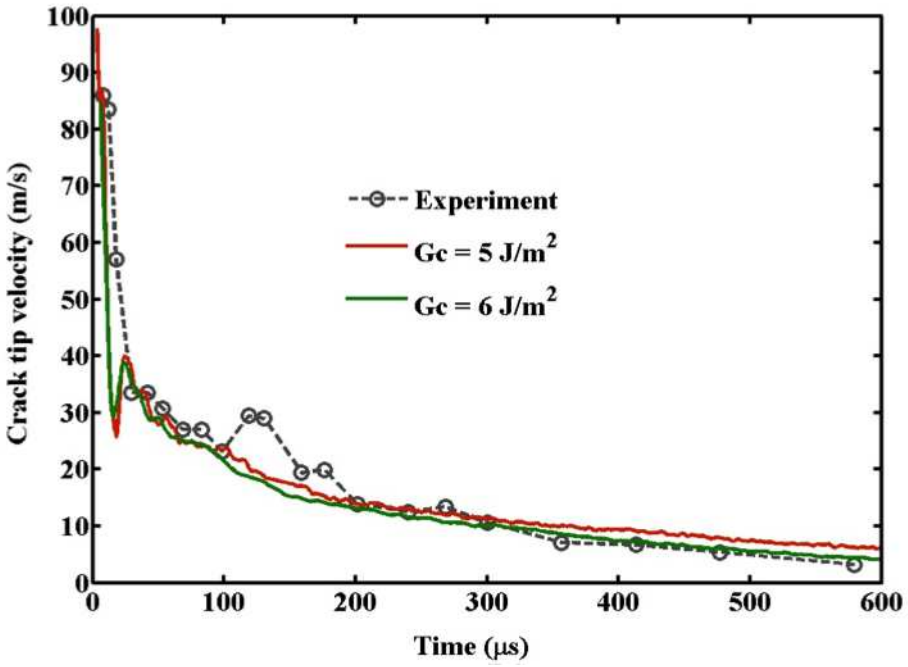

Figure 2.6 – Comparison between numerical predictions and experimental measurements of the crack tip velocity history. The simulations were conducted for two values of the interface fracture toughness (*Taken from [11]*).

Chapter 3

Residual Stresses

An inherent problem with most thin film manufacturing techniques is the presence of residual stresses induced by various extrinsic (manufacturing process, thermal mismatch, etc.) and intrinsic processes (grain size, microstructure, etc.). The residual stress levels can be high enough to cause the spontaneous delimitation of the film and it is utilized in certain experiments to gauge adhesion by inducing failure at the interface of interest [23, 41]. Residual stresses affect the mechanics of delamination as the recovered residual strain energy increases the energy available for fracture [23]. Residual stresses and stress gradients also affect the final shape of the delaminated film, as shown in Figure 3.1 obtained after the laser-induced delimitation of a set of patterned Al films deposited on Si [4]. Finally, residual stress may also affect the mode mixity of the interface failure, thereby affecting the fracture toughness predictions [23]. Investigating the role played by residual stresses on the dynamic delamination event is therefore essential to assess their contribution to the fracture toughness value extracted from the test. The investigation of the role played by residual stresses in the dynamic delamination test is the focus of the present chapter.

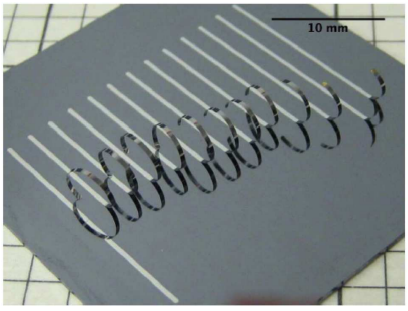

Figure 3.1 – Aluminum films on silicon substrate exhibiting the typical curl up observed in films due to the presence of residual stresses (*Taken from [11]*).

3.1 Modeling and Implementation

Upon release, residual stresses present in the film change the axial length and shape of the film. Arbitrary residual stress distributions can be resolved into equivalent axial force and bending moment, which can thus be used to simulate the effect of these stresses on the delamination process. The stress distribution across the thickness can be quite complex and varies widely with the material system and the manufacturing process parameters. The complex state of stress (σ_R) across the thickness can be modeled as a summation of polynomial distributions [42, 34] (Figure 3.2) as

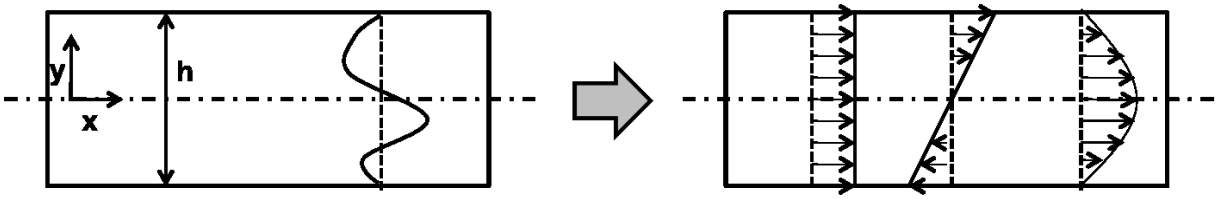

Figure 3.2 – Representation of a complex residual stress state by a superposition of polynomial stress distributions.

$$\sigma_R = \sum_{i=0}^{N} \sigma_i \left(\frac{y}{h/2}\right)^i, \tag{3.1}$$

where y is the ordinate value across the lateral thickness direction ($y \in \left\{\frac{-h}{2}, \frac{h}{2}\right\}$), h is the thickness of the film, σ_i is the stress level associated with the polynomial distribution and i represents the order of the polynomial distribution. A value of zero for i represents a uniform axial load while a value of one for i corresponds to a linear stress gradient across the thickness. The equivalent axial load (P_R) due to the combination of these polynomial stress distributions is

$$P_R = \int_A \sigma_R \, dA = b \int_{\frac{-h}{2}}^{\frac{h}{2}} \sum_{i=0}^{N} \sigma_i \left(\frac{y}{h/2}\right)^i dy = \frac{bh}{2} \sum_{i=0}^{N} \frac{\sigma_i}{i+1}[1 + (-1)^i], \tag{3.2}$$

where A and b are the cross-sectional area and width of the film, respectively. Similarly, the equivalent moment (M_R) due to the residual stresses is given by

$$M_R = \int_A \sigma_R y \, dA = b \int_{\frac{-h}{2}}^{\frac{h}{2}} y \sum_{i=0}^{N} \sigma_i \left(\frac{y}{h/2}\right)^i dy = \frac{bh^2}{4} \sum_{i=0}^{N} \frac{\sigma_i}{i+2}[1 - (-1)^i]. \tag{3.3}$$

As expected, the equivalent axial force results from the even polynomial distributions while the equivalent moment arises from the odd polynomial distributions.

The finite element formulation is essentially the same as that described in the previous chapter, except for the definition of the axial stress entering the principle of virtual work that describes the dynamic response of the nonlinear beam. The stress state in the film is now expressed as a superposition of the contribution associated with the external load (σ_{in}), with the residual axial force (σ_{Rax}), and with the residual axial moment (σ_{Rmom}).

$$\sigma = \sigma_{in} + \sigma_{Rax} + \sigma_{Rmom}. \tag{3.4}$$

This general expression for the stress state is then plugged into the weak integral form of the dynamic beam equation (2.15). Upon taking the appropriate variational derivatives, we get the required internal force vector and the consistent tangent matrix needed for the finite element implementation, a process that is detailed in Appendix B.

3.2 Verification

The formulation and implementation are verified by comparing the numerical predictions against analytical results of classical quasi-static and dynamic test problems. Static load tests are performed to ensure that the appropriate loading is generated when the residual stress is decomposed and applied as a series of polynomial distributions. The arbitrary residual stress state is decomposed into a series of polynomial distributions of increasing order. As made apparent in the previous section, the even polynomial distributions generate only an equivalent axial load while the odd distributions yield only an equivalent moment load. For the static validation study, a meter-long cantilever beam with a square cross-section of length 25 *mm* is used. The beam material is steel with the Young's modulus set to 210 *GPa* and a Poisson's ratio of 0.3.

The simplest case, which involves a net axial load, results only in the axial extension of the beam. The impact of having residual stresses that generate a net bending moment is evaluated by utilizing a linear stress distribution of magnitude 100 *MPa* resulting in a moment of 260.4 *Nm*. The linear variation causes a net positive moment causing the beam to curl up as apparent in Figure 3.3. As apparent there, the numerical results match exactly with that of the analytical prediction.

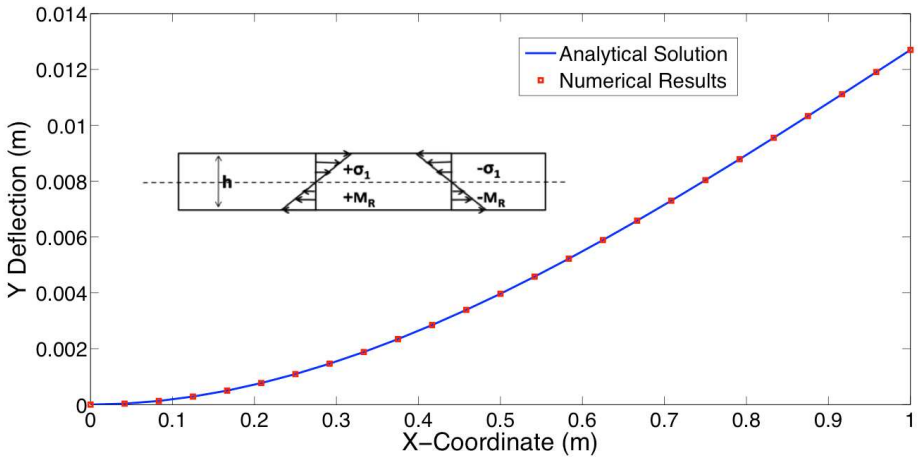

Figure 3.3 – Static verification test: Beam bending associated with a uniform residual stress gradient. The numerical values of the beam deflection match exactly the analytical calculations.

To verify the implementation of residual stresses in a dynamic problem, we simulate the classical problem of an axially loaded double cantilever beam with a transverse impulse load at the mid-point. An axial load acting on the beam serves to simulate the effect of residual stress. The analytical solution for this particular problem is obtained by assuming the solution to be harmonic as described in the book by Graff [43]. The solution for the transient deflection of the beam, $w(x,t)$, is given by

$$w(x,t) = \frac{2P}{\rho A l} \sum_{n=1,3,5\ldots} \left\{ \frac{[-1]^{\frac{n-1}{2}} sin(\alpha_n x) sin(\omega_n^2 + \eta_n^2)^{\frac{1}{2}} t}{(\omega_n^2 + \eta_n^2)^{\frac{1}{2}}} \right\}, \tag{3.5}$$

where P denotes the transverse impulse load, T the axial load applied to the beam, ρ the density of the material, A the cross-sectional area, and l the beam span. The other terms in the equation are defined as

$$\alpha_n = \frac{n\pi}{l}, \tag{3.6}$$

$$\omega_n^2 = \frac{EI}{\rho A} \alpha_n^4, \tag{3.7}$$

$$\eta_n^2 = \frac{T}{\rho A} \alpha_n^2. \tag{3.8}$$

The time step for the numerical model is set to the explicit formulation requirements,

which is determined using the CFL condition given by

$$\Delta t_{cr} \leq \frac{L^e}{\sqrt{E/\rho}}, \tag{3.9}$$

where L^e is the length of the smallest element and $\sqrt{E/\rho}$ the dilatational wave speed in the material. Even though the implementation is an implicit one, the time step is set to the explicit formulation requirements as the simulation is not computationally demanding. A comparison between numerical and analytical results is presented in Figure 3.4. The model consists of 40 beam elements with the impulse load applied during the first time step. The beam is subjected to an axial load T of 10,000 N with an impulse load P of 1000 N. In Figure 3.4, we compare the normalized deflection over the first few periods, showing a good match between the numerical and analytical results. The numerical predictions match especially well for the first time period, after which numerical and analytical results start to diverge progressively due to artificial period elongation.

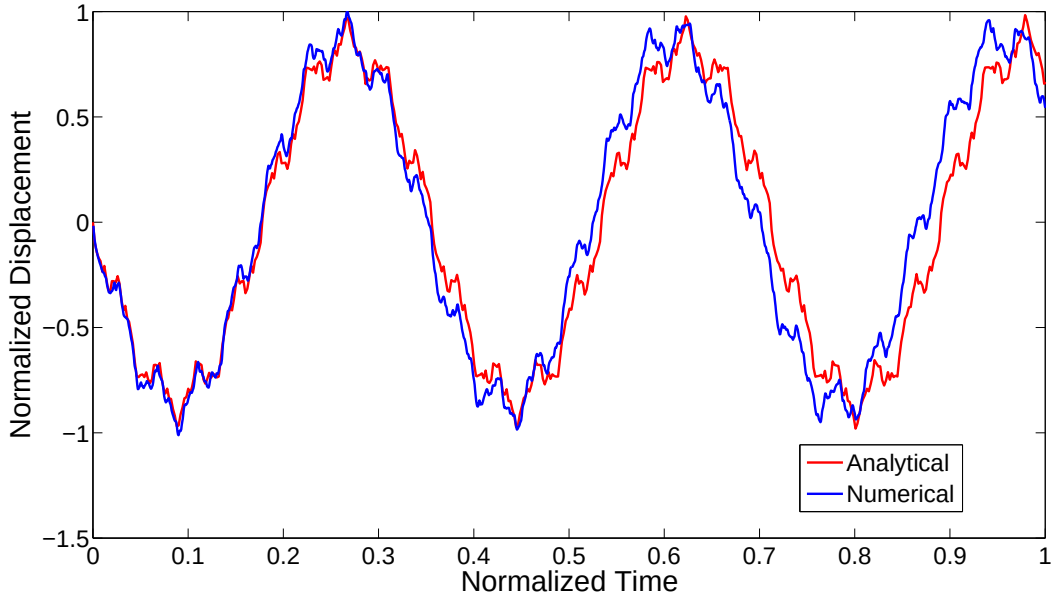

Figure 3.4 – Dynamic verification problem: normalized dynamic deflection of an axially pre-stressed beam (with an axial resultant load of 10,000 N) loaded with an impulse transverse load of 1000 N. Good agreement is obtained between analytical and numerical results.

3.3 Numerical Results

To analyze the impact of residual stresses on the dynamic delamination event, we adopt specimen dimensions and material properties similar to those of the film used in the experimental set-up, which consists of a 4.5 μm-thick and 300 μm-wide Al film deposited on a Si substrate. A 330 μm-long and 0.2 μm-thick weak adhesion layer of Au is sandwiched between the Al and Si at one of the ends of the Al film to form the pre-crack. The Au-Si interface has a significantly lower adhesion strength (50 MPa) than the Al-Si interface (300 MPa) [5]. The material property values used in the simulations are listed in Table 3.1. The pre-crack region is hit with a laser pulse of magnitude 1.5 GPa within a duration of

Table 3.1 – Material properties used in the simulations.

	Al	Au
Young's modulus, E (GPa)	70	77
Poisson's ratio, ν	0.33	0.42
Density, ρ (kg/m^3)	2710	19320
Critical traction, σ_c (MPa)	300	-
Critical opening displacement, δ_c (nm)	66.67	-

10 ns (Figure 3.5), which sets off a compressive stress wave. The stress wave is reflected from the top surface of the film as a tensile wave, loads the interface in tension and causes the failure of the Au/Si interface. As described earlier, the kinetic energy at the time of spallation present in the Au/Al bi-material film located above the pre-crack region is calculated using a 1D elastodynamic analysis and is found to be 171 J/m^2 [19]. The initial peeling velocity of the de-bonded film is determined by Equation (2.17) as 147.5 m/s. The calculated initial peeling velocity is applied as an initial condition to nodes located in the pre-crack region of the model to simulate the laser pulse loading. A convergence study was performed by Tran et al. [19] and an element size of 2 μm was found to be appropriate. The time step size adopted for the implicit simulation is set to 11 ns, about 30 times the explicit time step size calculated using the CFL condition (Equation (3.9)).

The residual stresses present in thin films can be measured in a number of ways, including the wafer-curvature technique, the bending curvature measurement of a micro-cantilever, and X-ray diffraction techniques [23]. Most of these techniques estimate only the average or mean residual stress and the linear-gradient residual stress across the thickness of the film as it is quite difficult to get the exact variation of the residual stresses across the thickness. Kandula et al [4] used the wafer-curvature technique to measure the mean residual stress in a 2.8 μm-thick blanket Al film deposited on a 4 μm-thick Si substrate and found it to be 15 MPa. However it has been reported in literature [44, 45]

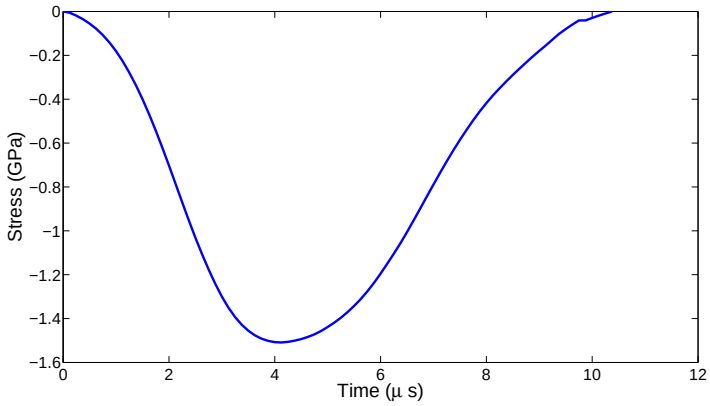

Figure 3.5 – Temporal profile of the laser-induced stress pulse with a rise time of 4 *ns* and a peak amplitude of 1.5 *GPa*.

that Al films can develop mean stresses as high as 230 *MPa*. To fully reflect a large range of residual stress values, we perform numerical simulations using residual stress values ranging from -300 to 300 *MPa*.

3.3.1 Effect of Mean Residual Stress

In this first study, we quantify the effect of mean residual stresses on the dynamic delamination event. The release of the residual stress in the delaminated portion of the film provides additional energy for failure. A portion of the recovered energy is channeled into the failure process increasing the delamination length as apparent in Figure 3.6 where the evolutions of the crack length are compared for various residual stress levels. As apparent there, large values of the residual stress affect the final extent of the crack, but the sign of the mean residual stress does not affect the propagation of the crack, as the amount of energy recovered is the same for tensile or compressive stress.

The additional energy release rate due to the relaxation of the mean residual stress for the case of a steady state delamination process has been estimated using simple energetic consideration as [4, 46]

$$G_P = \frac{1-\nu^2}{2Eh} P_R^2, \tag{3.10}$$

where ν is the Poisson's ratio, E the Young's modulus and h the thickness of the film.

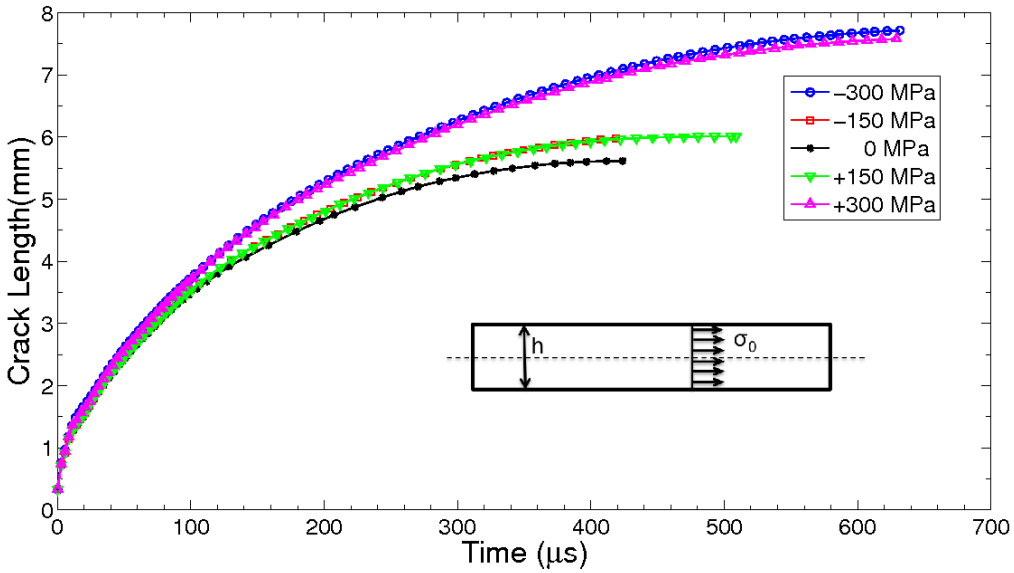

Figure 3.6 – Effect of mean stress amplitude σ_0 on the delamination crack propagation for residually stressed Al films with thickness of 4 μm and pre-crack length of 300 μm. The amplitude of the stress pulse is 1.5 GPa with a rise time of 4 ns.

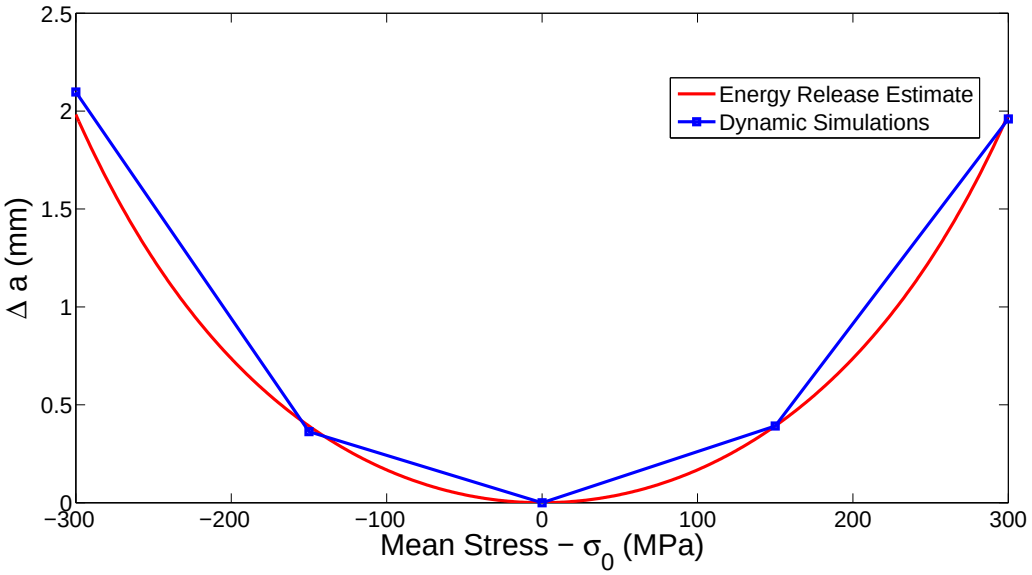

Figure 3.7 – Additional crack growth (Δa) resulting from mean residual stresses. The square symbols denote numerical results obtained from the dynamic delamination simulations, while the red curve corresponds to the static energy release rate estimate (Equation (3.10)).

The energy release expression inherently assumes that all the recovered energy is channeled into the failure process. Using this simple expression for the energy release rate, we

can determine the expected additional crack advance for the film, which are compared to the numerical prediction in Figure 3.7. As apparent in that figure, the predictions of the simple relation compare quite favorably with the results of the dynamic simulations. Note again that the quadratic nature of the relation indicates that the mean residual stress must be sufficiently large to affect substantially the dynamic delamination event. As expected, the mean residual stress does not affect the shape of the delaminated film at the time of crack arrest, as demonstrated in Figure 3.8.

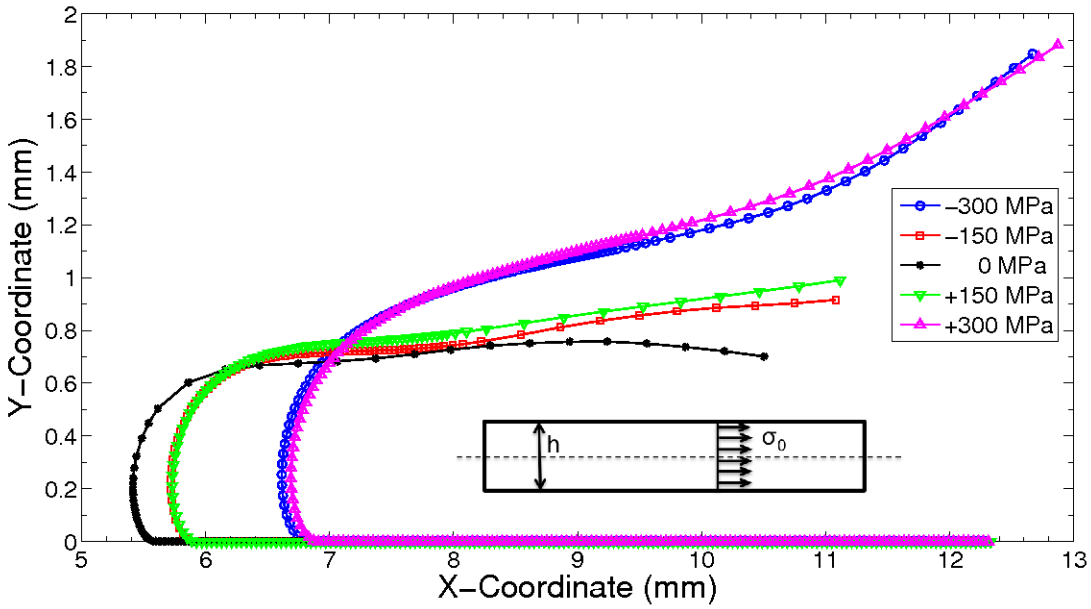

Figure 3.8 – Delaminated shape of the film after 400 μs under various mean stress levels. As expected, the films do not exhibit the typical curl-up observed in experimental testing as apparent in Figure 3.1.

The residual stresses have an effect on the mode mixity of the failure process. The tensile stress wave reflection from the top surface of the film creates a load normal to the interface causing a failure which is predominantly mode I. The average residual stresses when released adds a shearing component to the failure process. The effect of the residual stress level on the mode mixity factor (η_I), defined as the ratio of tensile (mode I) fracture energy to the total fracture energy, is presented in Figure 3.9. Higher mean stress levels induce a significant shearing component to the failure process with the mode mixity level of the order of 0.65 for the -300 *MPa* case.

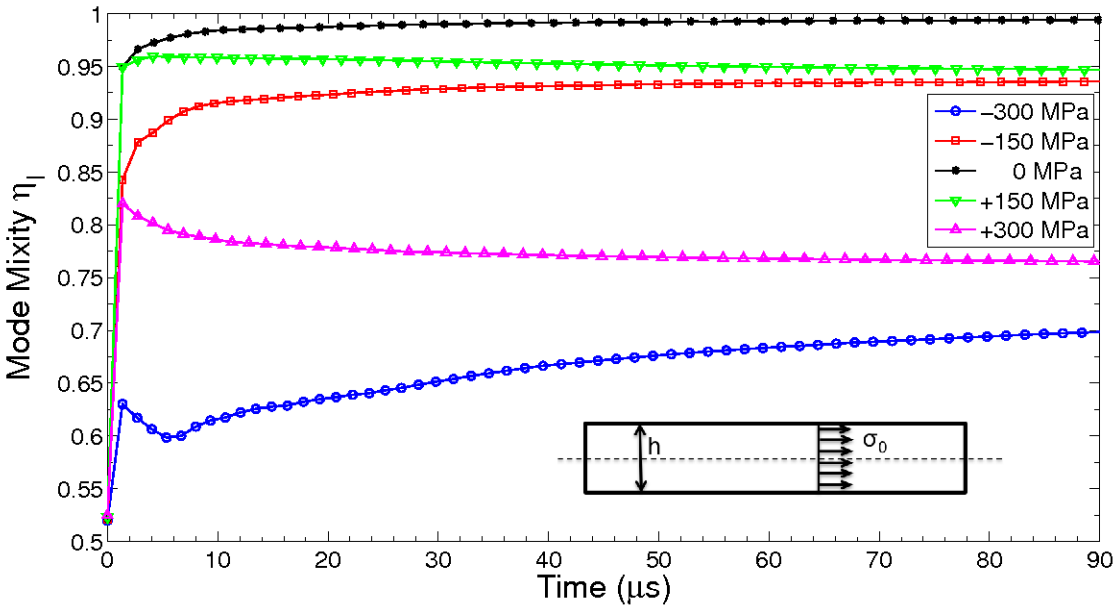

Figure 3.9 – Evolution of the tensile fraction (η_I) of the total fracture energy for various levels of mean residual stress σ_0, showing the increasing mode mixity of the failure process under high residual stress levels.

3.3.2 Effect of Residual Stress Gradient

We now focus our attention on the effect of residual stress gradients across the thickness of the film, which gives rise to a bending moment loading as described in Section 3.1. The moment loading arising from the linear stress gradient is termed positive if it causes the beam to bend up in the positive y direction as indicated in Figure 3.10 and negative if the bending is of the opposite nature. The crack length evolutions obtained for different stress gradients across the thickness are compared in Figure 3.10. As expected, positive residual moments, which cause the film to bend upward, facilitate the propagation of the delamination front, while negative moments tend to impede the crack growth. But overall, the impact on the final extent of the crack is very limited.

The additional energy release rate associated with the release of the stress gradient can again be estimated using simple energetic considerations of a steady state loading case as [46]

$$G_M = \frac{1-\nu^2}{2Eh}\left(\frac{12M_R^2}{h^2}\right), \tag{3.11}$$

where M_R is the resultant bending moment defined in equation 3.3. The effect of the residual stress gradients on the additional crack growth predicted by the dynamic finite element simulations are compared with the predictions of the steady state approximation

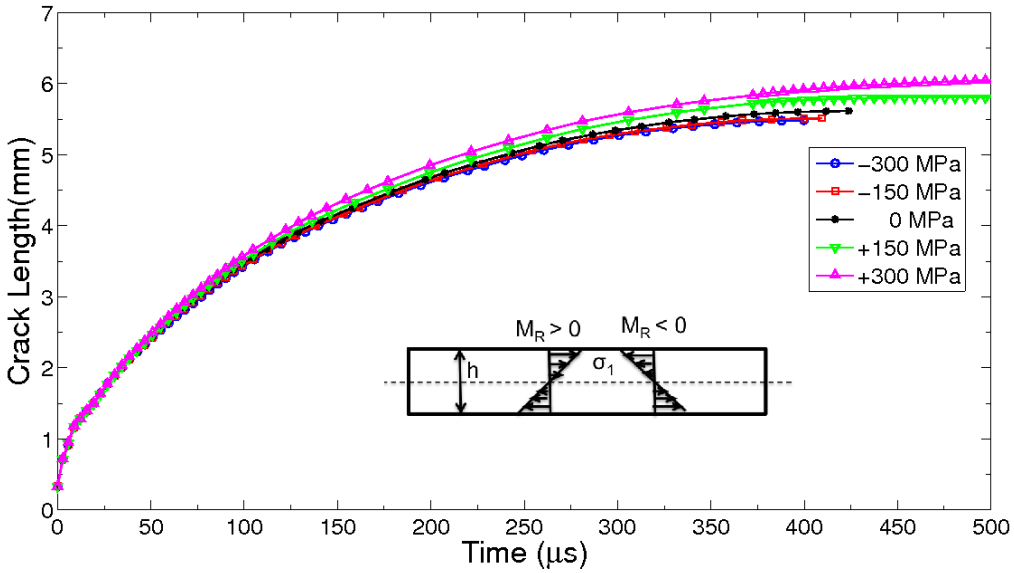

Figure 3.10 – Effect of the stress gradient on crack length evolution. The amplitude of the stress gradient is quantified by the value of the maximum axial stress σ_1 acting along the top and bottom surfaces of the film. Negative moments impede crack growth while positive moments promote additional delamination.

(Equation (3.11)) in Figure 3.11. It is apparent that the predictions of the energy release estimate do not match with that of the dynamic residual stress simulations. The energy release estimate predicts that the additional crack advance obtained is identical for both positive and negative linear stress gradients. The energy release estimate calculates the bending strain energy recovered should the residual stress gradients be released. The estimate does not differentiate between the nature of the distributions and tends to predict the same crack advance for both positive and negative distributions. But it is obvious that positive gradients, which cause the film to curl away from the substrate tend to promote crack growth, while negative gradients have the opposite effect. Thus unlike in the mean stress case, the crack advance predictions based on energy release estimates are not satisfactory and one must rely on numerical estimates instead.

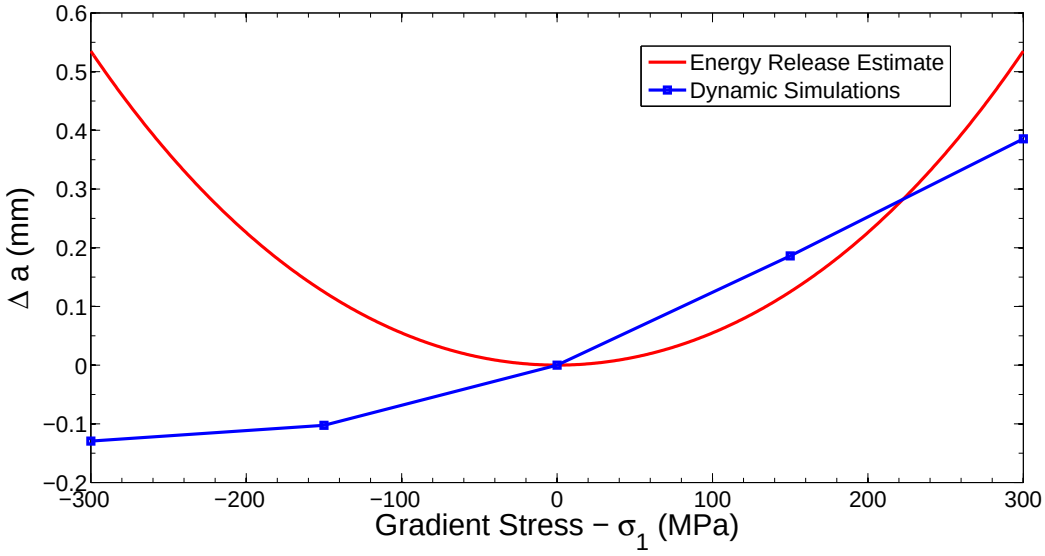

Figure 3.11 – Additional crack growth (Δa) resulting from residual stress gradients characterized by the maximum amplitude σ_1 with the sign convention illustrated in Figure 3.10. Comparison between numerical predictions obtained with the dynamic delamination solver (symbols) and the quasi-static energy balance (red curve).

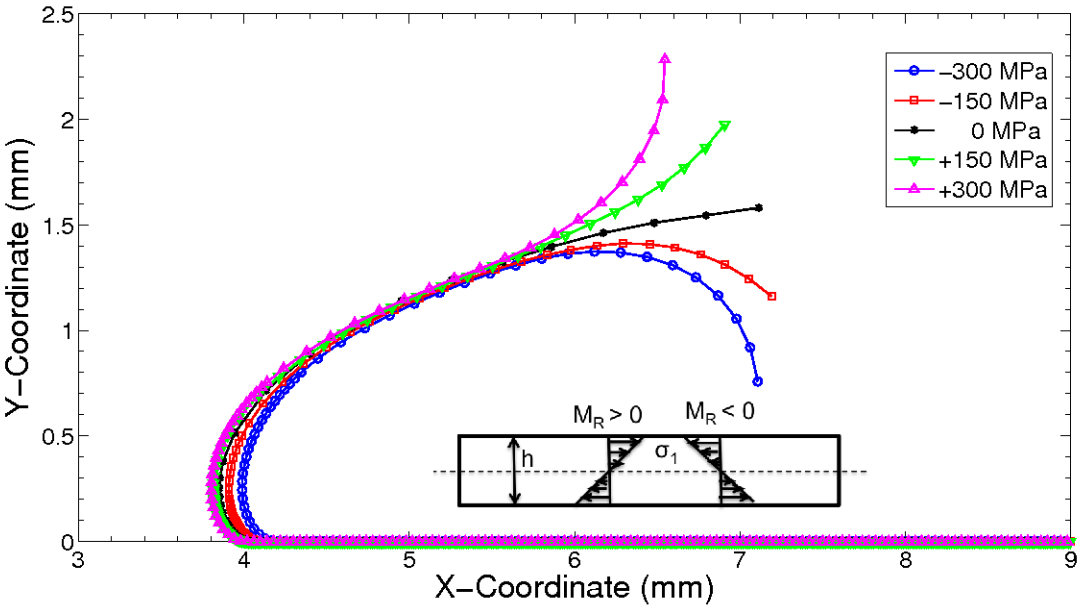

Figure 3.12 – Delaminated shape of the film after 150 μs under various gradient stress levels exhibiting the typical curl-up seen in testing (Figure 3.1).

As illustrated in Figure 3.12, delaminated films have been observed to curl up and adopt a distinctive shape. The residual stress variation across the thickness has been attributed

as the cause for the distinct shape observed during the delamination event. The effect of the stress gradient on the delaminated shape of the film at the end of 150 μs is presented in Figure 3.12, showing the expected curling of the film upward or downward depending on the sign of the residual bending moment.

Similar to the mean stress case, the effect of the gradients on the mode mixity of the failure process is studied by comparing the evolution of the tensile energy fraction (η_I) in Figure 3.13. The comparison reveals that the moment loading arising out of the gradient stresses hardly affects the mode mixity as it does not induce a shearing component at the film-substrate interface. The moment loading is predominantly normal to the surface and thus the failure process remains primarily of mode I nature.

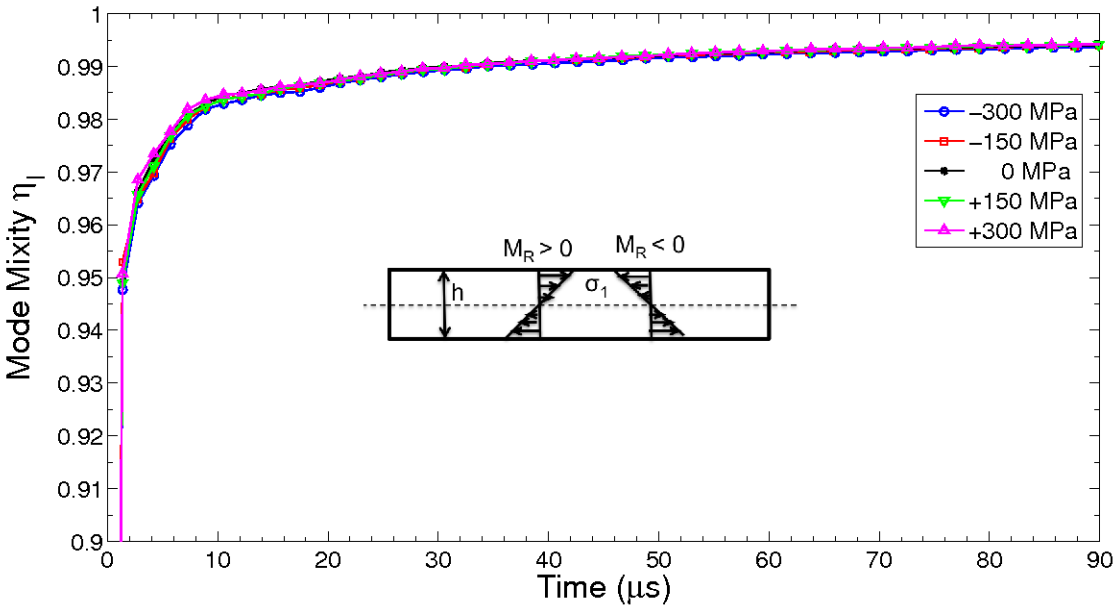

Figure 3.13 – Evolution of the relative mode I fracture energy (η_I) during the dynamic delamination event for five values of the residual stress gradient. The mode mixity is not affected by the gradient stress level and remains predominantly in mode I throughout the failure event.

Chapter 4

Dynamic Delamination of Polymer Films

Polymer films are being increasingly used in a variety of applications ranging from semiconductor devices, optical devices, implants, and packaging. In microelectronic devices, polymers have been most commonly used as insulators in the form of inter-level dielectrics, encapsulants, and materials for the packaging and housing of electronic equipment [47]. Recently, conducting polymers, which are made conducting by the use of dopants, have been developed and the use of polymers in microelectronics is only expected to grow [48]. Some of the attractive features of polymers include stability over a wide temperature range, ease of processing and handling, and good adhesion properties.

Polymer films in general have better adherence to silicon compared to metallic films. The interface toughness of polymer films on Si substrates can be in the order of 50 J/m^2, which is almost ten times the interface toughness of metallic films like aluminum [49]. Most of the uncross-linked polymeric materials gain their strength from entanglement between the chains. The polymeric chains form an entangled network that cannot pull apart when the material is in the glassy or semi-crystalline state, thereby resulting in better adhesion.

4.1 Challenges Associated with Laser-Induced Testing of Polymer Films

The higher toughness of polymer/Si interfaces makes laser-induced delamination testing of these films more challenging. Polymer films tend to fail cohesively due to the high stresses generated during laser loading as depicted in Figure 4.1(a). The polymer film over the pre-crack region (the shiny yellow region) has completely delaminated but no crack propagation has occurred over the tougher polymer-silicon region. Indeed, the film

failed cohesively when the delamination reached the strong interface, as confirmed with profilometer scan shown in Figure 4.1(b). The pre-crack region of gold spans 400 μm from 500 to 900 μm in the scan direction. When the crack front left the pre-crack region and reached the polymer-silicon interface, the film failed cohesively.

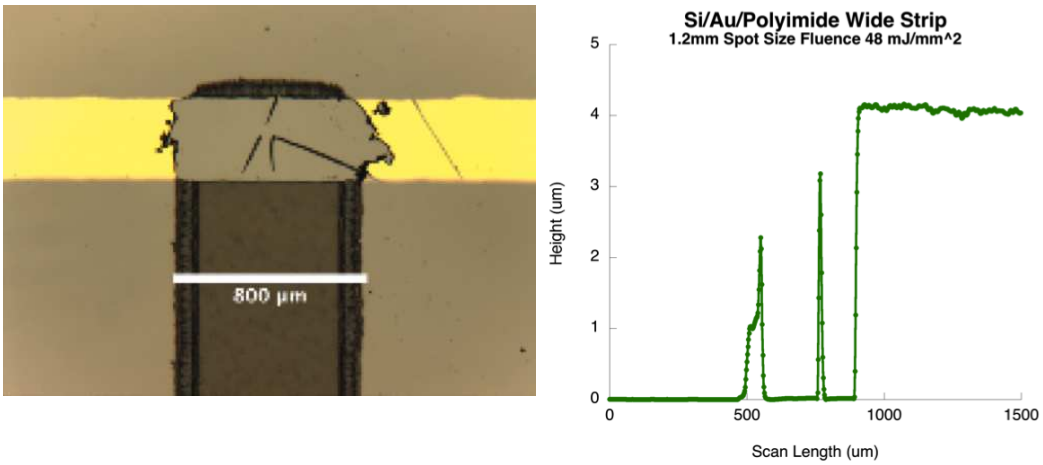

(a) (b)

Figure 4.1 – (a) Image of a laser-induced delamination test of a 4 μm-thick polyimide film on silicon. The film failed cohesively when the crack reached the tougher polyimide/Si interface. (b) Post-mortem profilometer scans showing the cohesive failure of the film. The film is 4 μm thick and has delaminated over the pre-crack spanning from 500 μm to 900 μm in the scan direction before failing cohesively (*Images courtesy of Martha Grady*).

The low density of polymer films, and the high stiffness mismatch between the polymer film and the substrate result in a smaller amount of stored kinetic energy in the pre-cracked region of the film compared to metallic films. As described earlier, the initial kinetic energy stored is responsible for the sustained delamination observed in laser-induced delamination testing. A comparison of the material properties of aluminum (Al) and polyimide (PI) is provided in Table 4.1. In Figure 4.2, the kinetic energy per unit area (K_{1D}) stored in the pre-crack region for Al and PI films are compared for films of various thicknesses. The pre-crack here consists of a 100 nm-thick layer of gold on top of which the films of various thicknesses are deposited. It is apparent that PI films have a substantially lower trapped kinetic energy than Al films.

This chapter details the efforts undertaken to enable the successful testing of polymer films. As mentioned above, laser-induced testing of polymer films poses significant challenges that need to be addressed. Firstly, the usefulness of adding an inertial layer to improve the amount of trapped kinetic energy and consequently the crack advance is

Table 4.1 – Material property comparison of Al & PI.

Property	Al	PI
Young's modulus, E (GPa)	70	3.5
Poisson's ratio, ν	0.33	0.35
Density, ρ (kg/m^3)	2710	1430

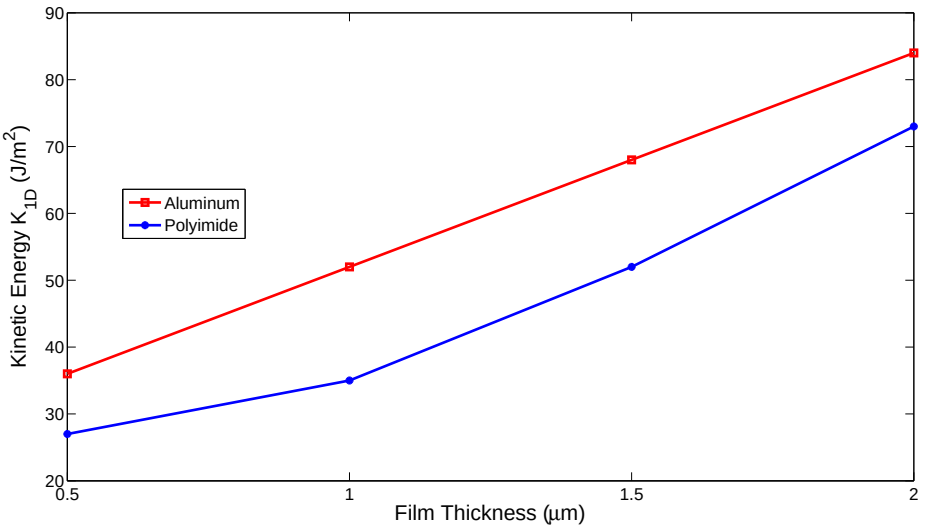

Figure 4.2 – Comparison of initial kinetic energy per unit area (K_{1D}) between Al and PI films of various thicknesses.

examined. Next, we evaluate the effectiveness of using a tapered shape for the pre-crack to avoid the observed cohesive failure of the film. The tapered region is expected to provide a more gradual transition into the tougher interface, reducing the axial stresses associated with the dynamic loading of the film. Finally we examine the impact of modifying the pre-crack geometry to improve testing efficiency by increasing the number of specimens tested.

4.2 Inertial Layer

The deposition of an inertial layer on top of the polymer film has been proposed to address some of the aforementioned problems associated with polymer film testing. An inertial layer increases the amount of kinetic energy trapped in the film, thereby increasing crack advance. An inertial layer can also prevent the film from failing cohesively by reducing the axial stress induced in the film. In this section, we thus investigate numerically the

role that an inertial layer might play in the dynamic delamination process. The film is now a multi-material film stack and hence changes need to be made to analyze the effect of inertial layers on film delamination.

4.2.1 Modeling Multi-Layered Film Stacks

The multi-material stack is modeled using 1D nonlinear beam elements with homogenized properties. Among the various homogenization theories available, we opt hereafter for the equivalent area method because of its simplicity. In this method, an equivalent cross-section is obtained by scaling the areas of the different film layers. First a reference layer is chosen and the beam is considered to be made up entirely of the material of the reference layer. The cross-sectional area of the other layers are then scaled according to the ratio of the moduli of the reference material and the corresponding layer, while keeping the thickness of the film stack constant [50]. This process is schematically shown in Figure 4.3. The scaling of the cross-sectional area of the layers ensures that the axial stiffness of the equivalent beam represents that of the film stack. Once the cross-section is defined, we

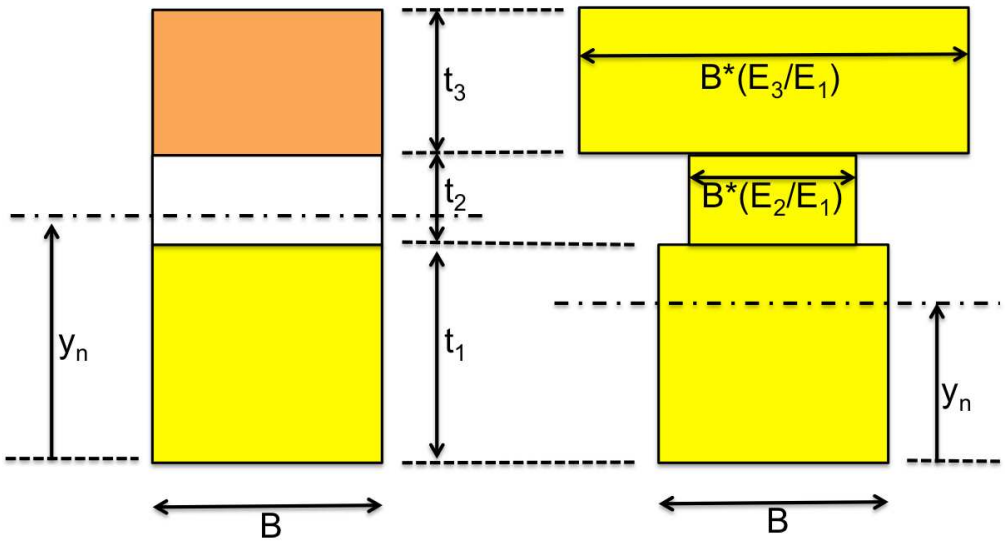

Figure 4.3 – Schematic of the scaling process utilized to determine the equivalent cross-section of a multilayered beam. The thickness of the various layers is preserved while the width is scaled by the modulus ratio. In the schematic, the reference layer is the first layer.

can determine the equivalent bending properties. The new cross-section is not symmetric about the central plane and hence the neutral axis is no longer at the center line of the beam. The new position of the neutral axis can be determined using the requirement that

the integral representing axial forces be zero in the case of pure bending [50]

$$\int_A (y - y_n)\, dA = 0. \tag{4.1}$$

By substituting the geometric properties of the respective layers, a general expression for the neutral axis of a n-layered film stack can be determined as [50]

$$y_n = \frac{1}{2}\left[\frac{\sum_{r=1}^{n} E_r t_r \left\{2\left(\sum_{i=1}^{r} t_{i-1}\right) + t_r\right\}}{\sum_{j=1}^{n} E_j t_j}\right], \tag{4.2}$$

where E_i and t_i denote the stiffness and thickness of layer i.

Once the neutral axis location is determined, the equivalent moment of inertia can be obtained using the following requirement about the second moment of area:

$$\int_A (y - y_n)^2\, dA = 0. \tag{4.3}$$

In a similar fashion to that of the neutral axis case, the substitution of the relevant geometric properties yields a general expression of the form

$$I = \frac{b}{3}\left[y_n^3 + \frac{1}{E_1}\sum_{r=2}^{n} (E_{r-1} - E_r)\left\{\sum_{i=1}^{r-1} t_i - y_n\right\}^3\right]. \tag{4.4}$$

The presence of a multi-material film stack also requires modifications to the manner in which the stresses in the film are calculated as each layer of the composite beam experiences different axial stresses. The strain is continuous across the beam cross-section and is determined from the displacement solution obtained using the homogenized properties. The axial stresses are discontinuous due to the material mismatch and are obtained with the following procedure, first illustrated in the case of a bi-material beam and then generalized for a multi-material beam. Using Hooke's law we determine that [51]

$$\varepsilon_1^{ax} = \varepsilon^{ax} = \frac{\sigma_1^{ax}}{E_1}, \tag{4.5}$$

$$\varepsilon_2^{ax} = \varepsilon^{ax} = \frac{\sigma_2^{ax}}{E_2}. \tag{4.6}$$

Eliminating ε^{ax}, we get

$$\frac{\sigma_1^{ax}}{E_1} = \frac{\sigma_2^{ax}}{E_2}. \tag{4.7}$$

The total load P must equal the stress multiplied by the respective area, yielding

$$P = A_1\sigma_1^{ax} + A_2\sigma_2^{ax}. \tag{4.8}$$

The combination of the two equations leads to

$$\sigma_1^{ax} = \frac{P}{A_1 + A_2\left(\frac{E_2}{E_1}\right)}, \tag{4.9}$$

$$\sigma_2^{ax} = \frac{P}{A_1\left(\frac{E_1}{E_2}\right) + A_2}. \tag{4.10}$$

This simple analysis can be extended to enable the calculation of the axial stress in a

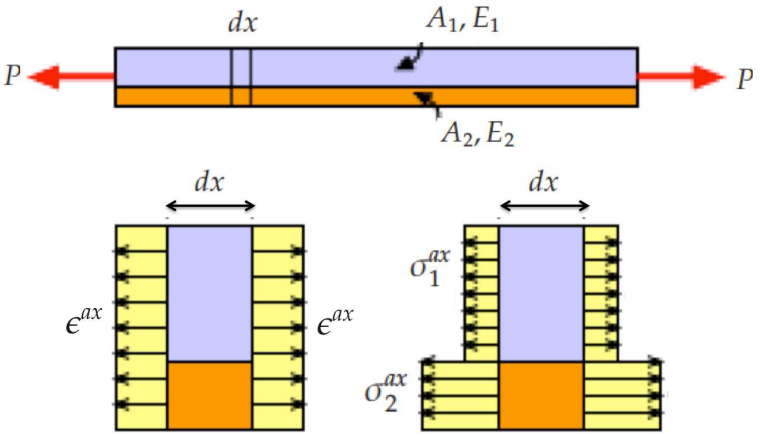

Figure 4.4 – Schematic of the state of axial stress in a bi-material beam, showing the continuity of axial strain and discontinuity of axial stress across the layers.

n-layered beam stack as

$$P = A_1\sigma_1^{ax} + A_2\sigma_2^{ax} + \ldots + A_n\sigma_n^{ax}, \tag{4.11}$$

$$\sigma_n^{ax} = \frac{P}{A_1\left(\frac{E_1}{E_n}\right) + A_2\left(\frac{E_2}{E_n}\right) + \ldots + A_n}. \tag{4.12}$$

Thus, from the displacement solution obtained using the homogenized properties, one can determine the axial strain. Using the strain and Equation (4.11), we can determine the axial load as [51]

$$P = A_1\varepsilon^{ax}E_1 + A_2\varepsilon^{ax}E_2 + \ldots + A_n\varepsilon^{ax}E_n, \tag{4.13}$$

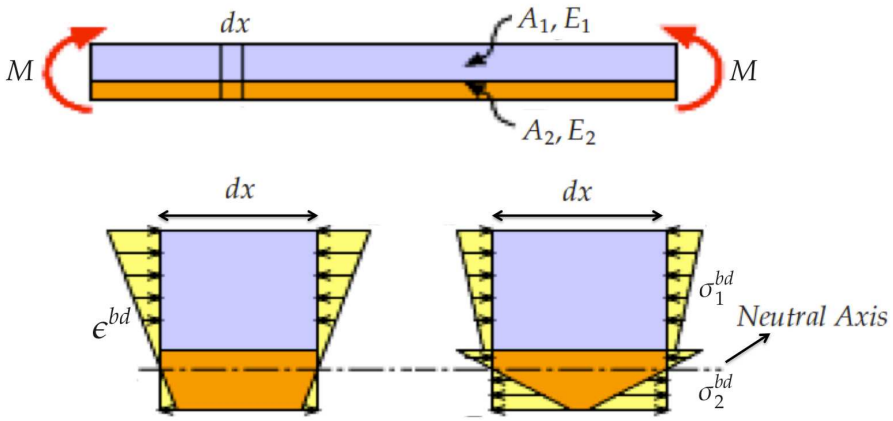

Figure 4.5 – Schematic of the state of bending strain and stress in a bi-material beam, showing that the neutral axis is not at the central plane.

and, from Equation (4.12), the axial stress in each layer.

For the composite beam, the centerline of the beam is not the neutral axis and hence the bending of the beam is un-symmetric. The displacement results obtained using the homogenized properties are used to calculate the bending moment [51]. The bending stress in the composite beam can be found by using the moment equilibrium equation at any internal location as

$$\sum M_z = 0 \Rightarrow M_z = \int_{A_n} \sigma_n^{bd} y dA. \tag{4.14}$$

The bending strain is continuous across the different layers, but the stress is not. The stress in each material layer can be determined from the above expression as

$$\sigma_n^{bd} = -\frac{E_n}{E_{reference}} \frac{M_z y}{I}, \tag{4.15}$$

where I is the moment of inertia of the equivalent beam, M_z the bending moment of the equivalent beam and y the distance of the fiber from the neutral axis of the equivalent beam.

4.2.2 Verification

The implementation of the multi-layered beam formulation is verified using a test problem that consists of a cantilevered bi-material beam made of a 5 *mm*-thick layer of steel (E = 210 *GPa*) on top of a 25 *mm*-thick layer of Al (E = 70 *GPa*). The beam is 1 *m* long and is loaded by a tip load of 1000 *N*. The neutral axis of this combination is located at 18.25

mm from the bottom fiber. Using the formula derived in the previous section, one can easily determine analytically the state of stress at the root of the beam. The peak tensile bending stress occurs in the steel portion of the beam and has a value of 10.35 *MPa* while the peak compressive bending stress occurs in the Al portion of the beam and has a value of 5.25 *MPa*. The numerical solution obtained with the multilateral beam solver is shown in Figure 4.6 and shows perfect match with these analytical calculations.

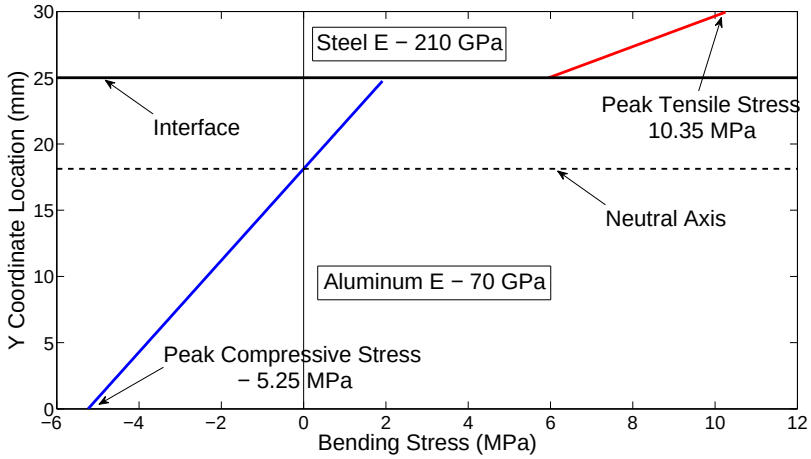

Figure 4.6 – Stress state in a bi-material cantilever beam made of Al and steel with a tip load of 1000 *N* showing the discontinuous nature of bending stress across the interface.

4.2.3 Studies with Multi-Layered Film Stacks

The primary aim of the inertial layer is to increase the kinetic energy trapped in the pre-crack portion of the film. The 1D elastodynamic solver is used to determine the kinetic energy trapped in the film for four potential metals. The metals and their essential properties are listed in Table 4.2. The effect of inertial layer material and thickness on the kinetic energy per unit area (K_{1D}) trapped in the pre-crack portion of the film is presented in Figure 4.7. As expected, the amount of kinetic energy is directly proportional to the density of material as silver (Ag) is seen to have the most K_{1D}. Also, the thicker the inertial layer, the more kinetic energy is stored in the film.

As Ag is determined to provide the most amount of trapped kinetic energy, the impact of adding Ag as an inertial layer is examined. Limitations on the amount of Ag that can be deposited restrict the inertial layer thickness to a maximum of 1 μm. The model consists of a pre-crack having 100 *nm*-thick gold layer with a 5 μm-thick PI film strip and an inertial

Table 4.2 – Material property comparison of candidate materials for the inertial layer.

Material	Modulus (GPa)	Density (kg/m^3)
Silver (Ag)	83	10490
Copper (Cu)	119	8940
Chromium (Cr)	279	7190
Al (Al)	70	2710

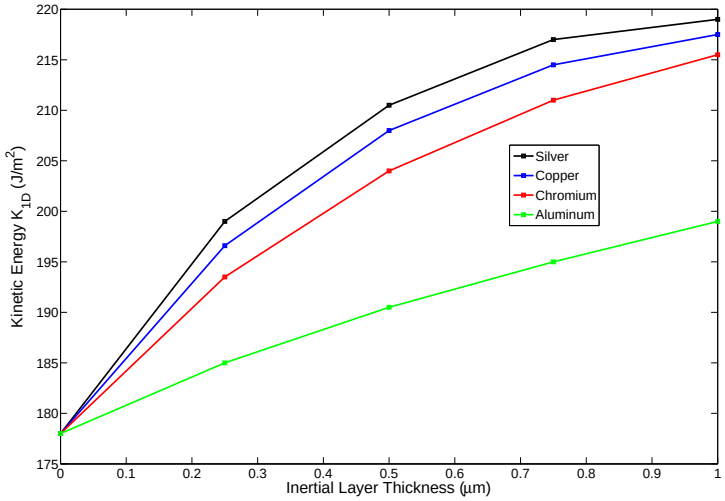

Figure 4.7 – Comparison of K_{1D} values obtained with the four candidate materials for inertial layers with varying thickness values.

layer made of Ag of varying thickness. The laser pulse load has a rise time of 5 ns with load amplitude of 1.5 GPa in all cases. The Au-silicon interface is weak and is assumed to have no interface toughness. The PI-silicon interface on the other hand is very tough and, based on toughness values reported in [49], is set to 50 J/m^2 with an interface strength of 300 MPa. Crack advance evolution curves are obtained for four different values of Ag layer thickness and they are compared to that obtained in the absence of an inertial layer in Figure 4.8. It is observed that, with the addition of an inertial layer, the crack advance increases substantially, by about 310 μm, compared to the case without inertial layer.

An interesting feature is that the crack advance obtained for the various thicknesses of Ag inertial layer are almost the same. This is due to the competing processes of the increased kinetic energy and the increased difficulty in spalling a larger mass of material. It is observed that the crack speed for thinner inertial layers is higher, but the thicker films have more trapped kinetic energy and hence the crack propagates for a longer period of time, eventually providing the same crack advance. In all cases though, the beneficial impact of the inertial layer on extending the crack growth is clearly observed.

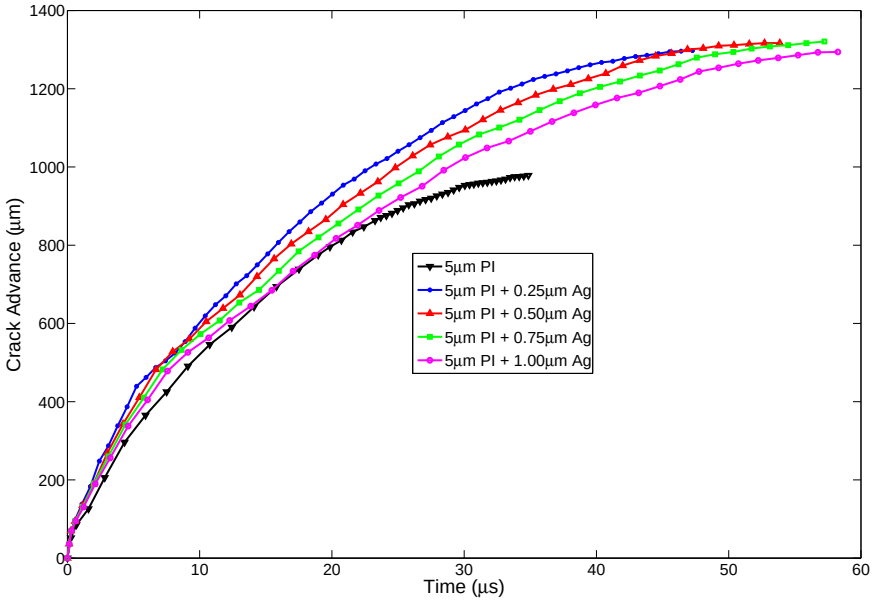

Figure 4.8 – Comparison of the crack advances obtained for a 5 μm-thick PI film with Ag inertial layers of varying thickness ranging from zero to 1 μm. The inertial layer is seen to help improve the crack advance by about 310 μm.

The addition of the inertial layer is also expected to lower the stresses induced in the PI film as the film is reinforced by the addition. As explained in the previous section, the axial and bending stress components can be calculated separately for each film stack component. The peak axial and bending stress induced in the PI film at any instant can be recorded. A typical result, obtained in the case of a 5 μm-thick PI film without inertial layer is shown in Figure 4.9, together with the evolution of the crack length during the onset of the delamination event. During the laser pulse loading phase, the film over the pre-crack lifts-off instantaneously resulting in the build up of large axial stresses in the film just beyond the pre-crack. The whiplash effect created by the instantaneous failure results in significantly higher crack speeds as well. As the delamination front grows, the delaminated film starts curling up and the axial stress levels decrease reaching a steady state. As the crack length increases, the impact of the whiplash effect is reduced as the film starts to curl resulting in slower crack speeds.

A comparison between the evolution of the peak axial stress in the initial phase of the delamination obtained the different thickness values of the inertial layer is presented in Figure 4.10 for various values of the inertial layer thickness. The peak axial stress drops significantly with the addition of the inertial layer. The 1 μm-thick inertial layer reduces the peak axial stress to 75 MPa from about 150 MPa in the case without the inertial

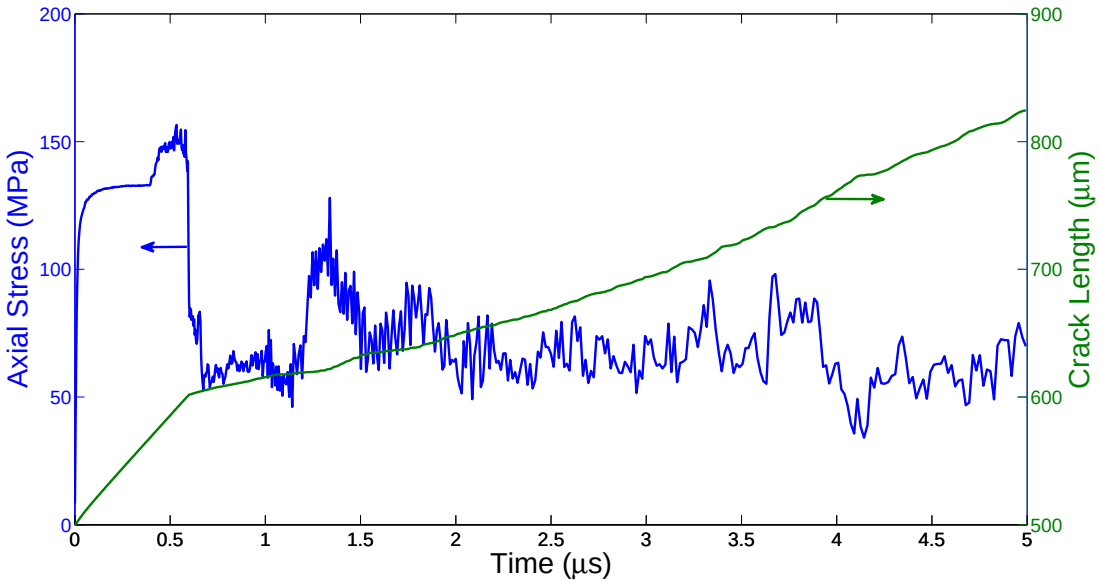

Figure 4.9 – Comparison of the crack advance and axial stress evolution for a 5 μm-thick PI film with an Au inertial layer of 100 nm. The axial stress peaks during initial lift-off of the pre-crack region, which is characterized by higher crack tip velocities as well.

layer. Figure 4.11 compares the peak bending stresses induced in the PI film during the delamination process. As expected, the bending stress induced during the initial loading pulse is substantially smaller. Also, the bending component of the axial stress does not appear to be changed much by the addition of the inertial layers. Comparing Figures 4.10 and 4.11, we observe that the peak axial stresses occur in the first few microseconds of the dynamic loading event, while the bending stresses are almost negligible during that time interval. The film at first fails due to the axial load followed by the curling up of the film away from the interface, which induces significant bending loads. Hence the bending stresses start building up later in the delamination process. The experimental observations corroborate this interpretation as the PI films fail cohesively during the initial laser loading phase, as depicted in Figure 4.1.

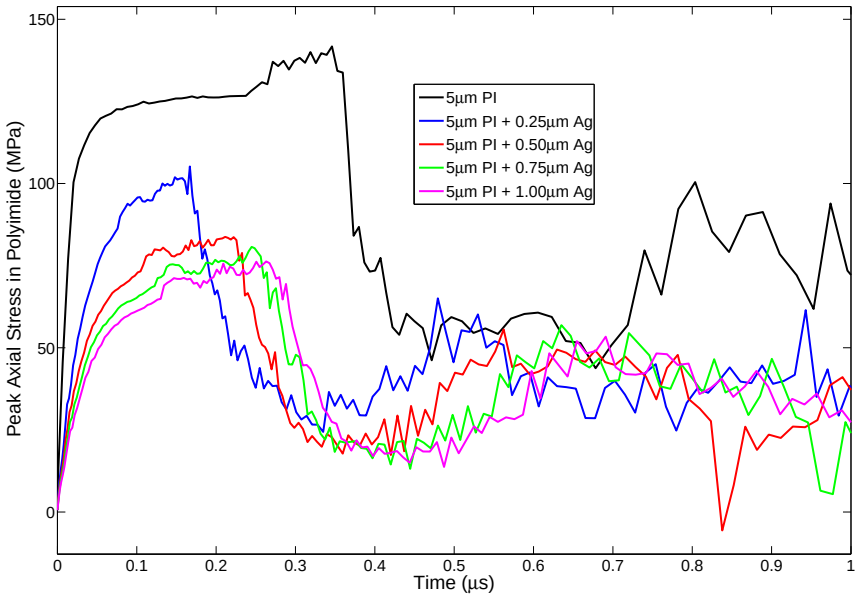

Figure 4.10 – Effect of inertial layer thickness on the peak axial stress induced in the film during the initial stages of the laser loading, showing how the presence of the inertial layer reduces the induced stress by up to 50%.

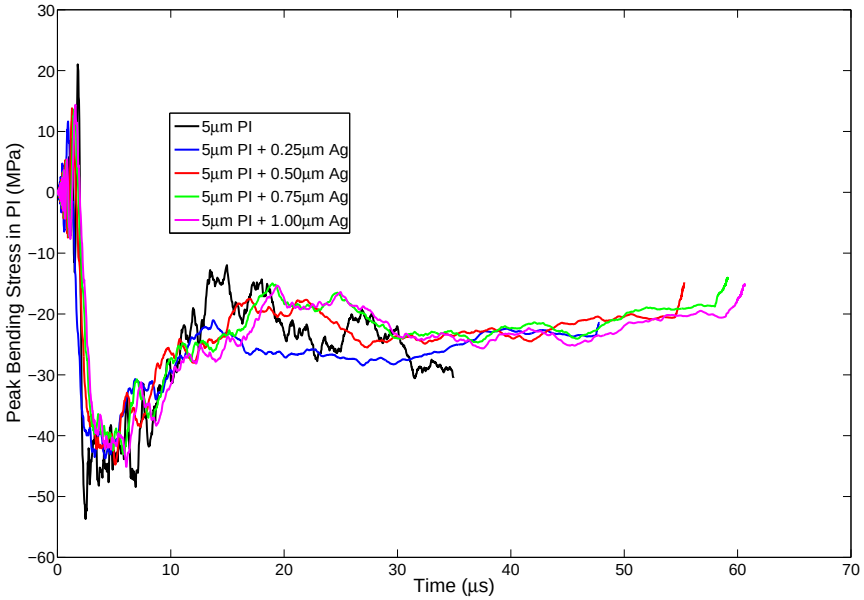

Figure 4.11 – Comparison of the peak bending stress induced in the PI film, showing a limited impact of the inertial layer.

4.3 Parametric Study

The toughness of the interface has an influence on the stresses generated during the delamination process. The interface toughness determines the crack advance and the manner in which the delamination occurs. The effect of the interface toughness on the peak axial stress developed is examined in the parametric study presented in this section. As mentioned previously, for the exponential traction-separation law used in this work, the interface toughness, defined as the area under the traction-separation curve, is given by

$$G_c = e\sigma_c\delta_c, \tag{4.16}$$

where σ_c is the critical interface strength, δ_c the corresponding critical opening displacement and e the natural logarithm value. One could vary the toughness either by changing the critical interface strength or the critical opening displacement. The study is done by changing both parameters. Again here the model consists of a 500 μm-long pre-crack with a 100 nm thick gold layer as weak adhesion layer, and with a 5 μm-thick PI film strip. The laser pulse load has a rise time of 5 ns with the load amplitude being 1.5 GPa. The Au-Si interface is assumed to have no toughness.

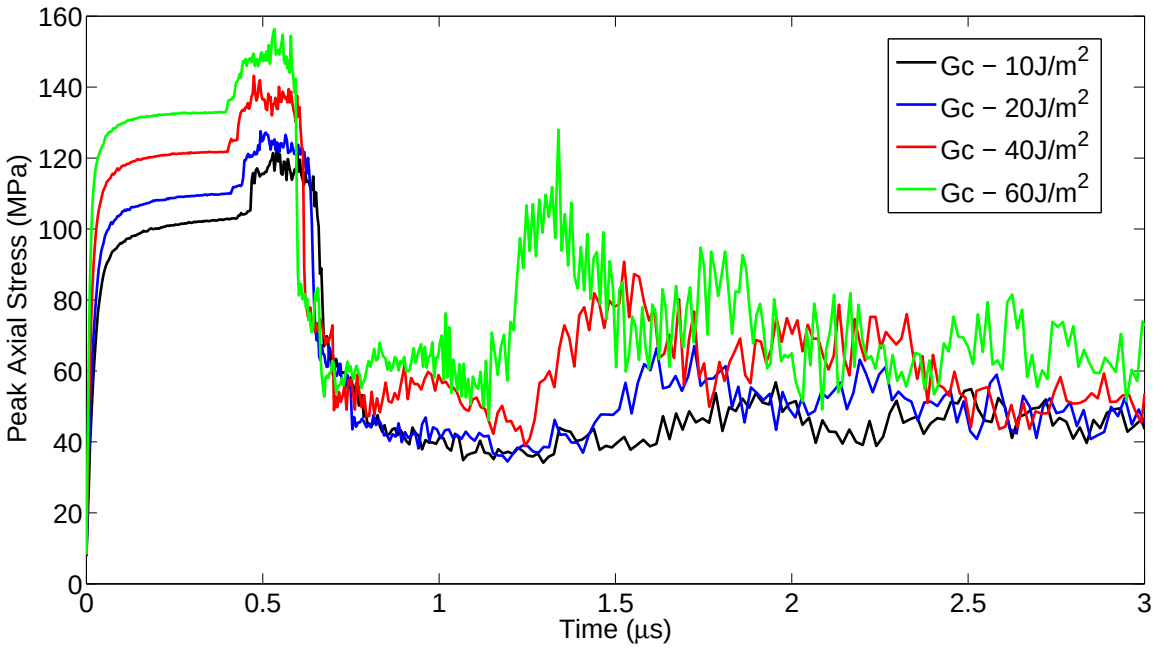

Figure 4.12 – Effect of fracture toughness G_c on the evolution of the peak axial stress in a 5 μm-thick PI film with varying interface strength σ_c.

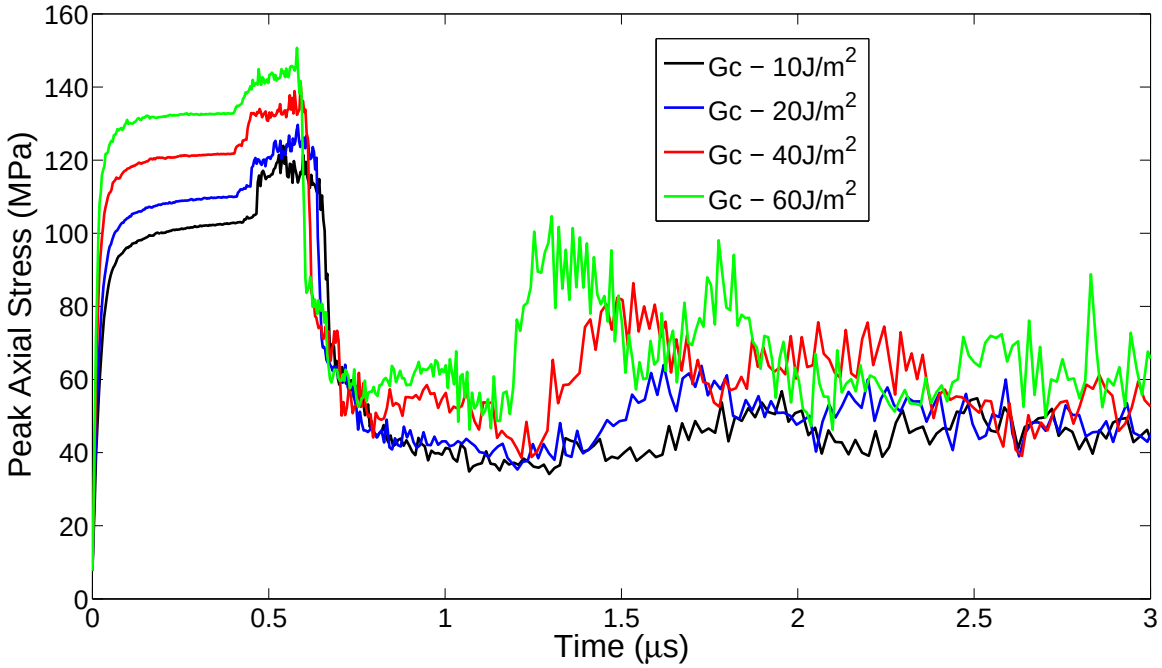

Figure 4.13 – Effect of fracture toughness G_c on the evolution of the peak axial stress in a 5 μm-thick PI film with varying critical opening displacement δ_c.

The impact on the axial stress in the film is depicted in Figure 4.12. It is apparent that the axial strength is strongly influenced by the interface toughness as the stress increase from 120 MPa for 10 J/m^2 to about 150 MPa for 60 J/m^2. Figure 4.12 represents the axial stress variation when the toughness is varied by changing the interface strength, while Figure 4.13 is obtained by changing critical opening displacement. It is apparent that the stresses developed are the same for both parameter variations and depend only on the toughness value.

The bending stress variation for different interface toughness values is depicted in Figure 4.14, whereby the results are obtained by varying the interface strength (σ_c). The bending stress variation obtained with the variation of critical opening displacement is identical to that of interface strength variation. Hence similar to axial stress variation, the bending stress is influenced only by the interface toughness value. It is quite apparent that the bending stress is influenced by the interface toughness, even though the bending stress component is not as significant as its axial counterpart. In summary, both the stress components show a strong dependance on the interface toughness, and hence the stresses induced in polymer films are certainly higher. In Figure 4.15, the crack advance curves for different interface toughness values are compared: as expected the crack advance is substantially less for tougher interfaces.

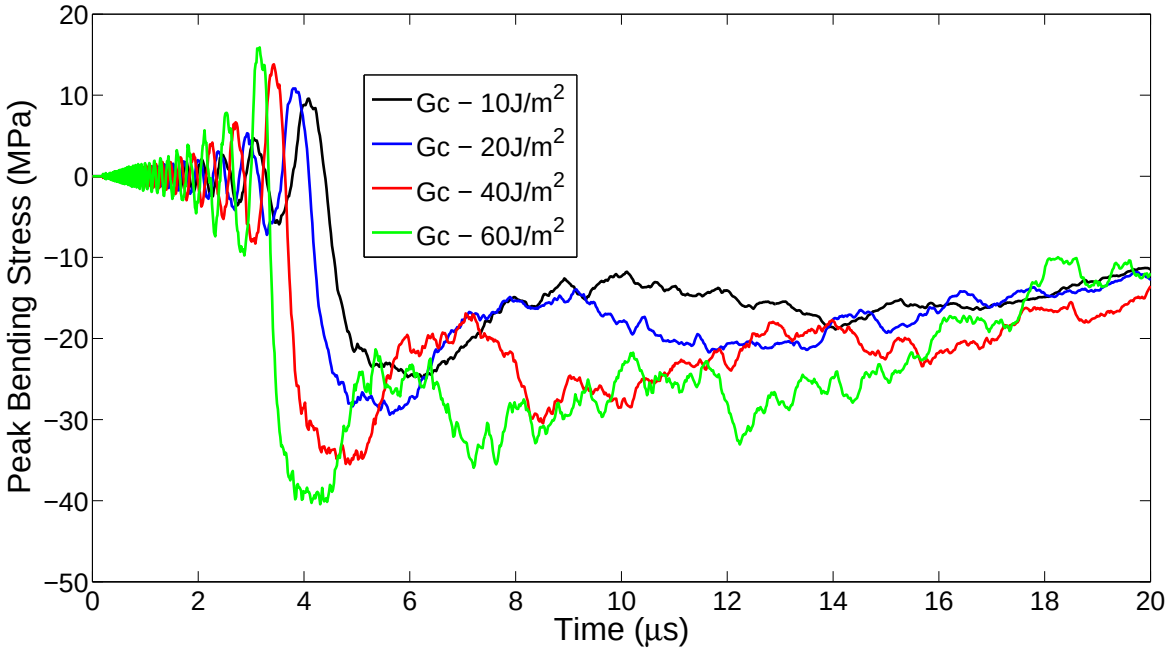

Figure 4.14 – Evolution of bending stress for a 5 μm-thick PI film with increasing values of toughness G_c obtained by varying the critical interface strength σ_c.

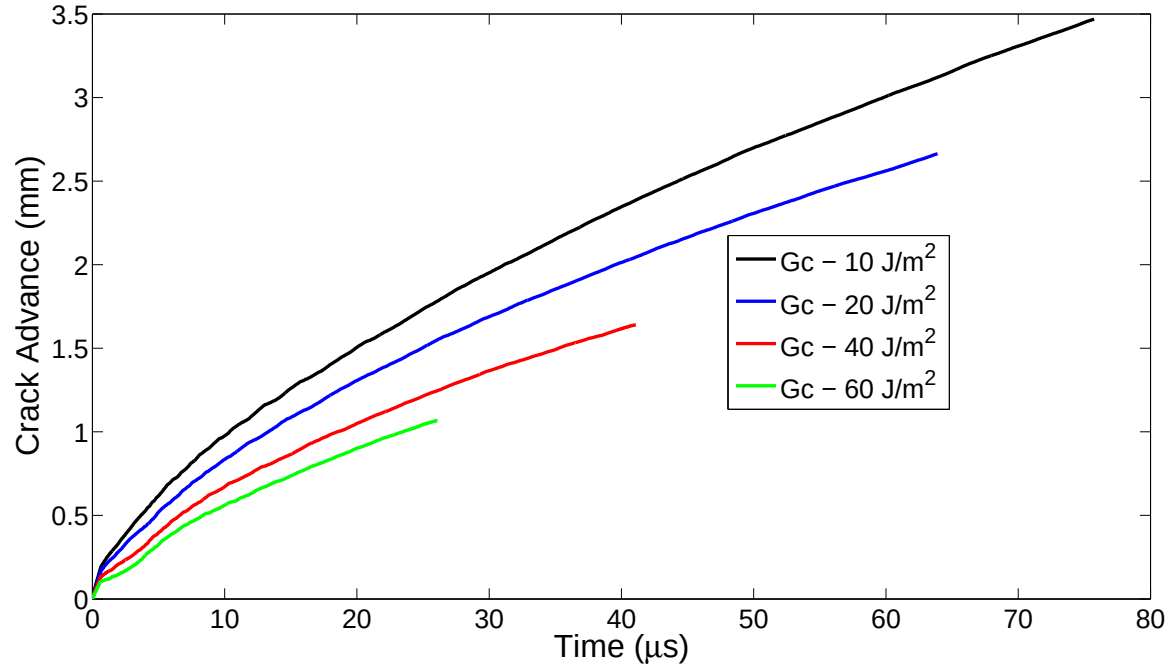

Figure 4.15 – Crack advance evolution for a 5 μm-thick PI film with increasing values of toughness G_c.

4.4 Pre-crack Geometry Modifications

One of the objectives of the study is to develop modifications in the specimen geometry, which might alleviate the problems associated with laser-induced testing of tough polymer films. As indicated earlier, the PI films were observed to fail cohesively when the crack advance reached the tougher interface. Here, the introduction of certain modifications to the pre-crack geometry to alleviate this problem is evaluated numerically. Modifications are also made to the pre-crack geometry to improve the testing efficiency. The impact of these modifications on the delamination process is examined as well.

4.4.1 Triangular Pre-Cracks

As depicted in Figure 4.1, polymer films are observed to fail cohesively when the crack advances beyond the pre-crack and reaches the strong interface between polymer and silicon. The pre-crack geometry is a rectangular one, which results in an abrupt transition from the weak gold-silicon interface to the strong polymer-silicon interface. In order to have a more gradual transition to the strong interface, modifications in the form a triangular section at the end of the pre-crack are considered. This approach is inspired from super-layer tests [52] that use such geometries to obtain quasi-static interface toughness data. The new pre-crack geometry shown in Figure 4.16(a) ensures a more gradual transition to the strong interface.

The approach to model the triangular pre-crack mirrors that of the inertial layer modeling. The triangular pre-crack region has the influence of both the strong polymer-silicon interface and the weak gold-silicon interface but in varying proportions along its length. The properties of the film in the triangular region are a combination of both the strong and weak interfaces and are assumed to be obtained based on a weighted average, with the surface area as the weighting parameter. The process is schematically depicted in the Figure 4.16(b). For each element the area encompassed by the two different interfaces are calculated and used for the weighted average parameter calculations. The key properties in the triangular region can then be defined as

$$G_c(x) = G_c^{Weak}\hat{A}^{Weak} + G_c^{Strong}\hat{A}^{Strong}, \tag{4.17}$$

$$\rho(x) = \rho^{Weak}\hat{V}^{Weak} + \rho^{Strong}\hat{V}^{Strong}, \tag{4.18}$$

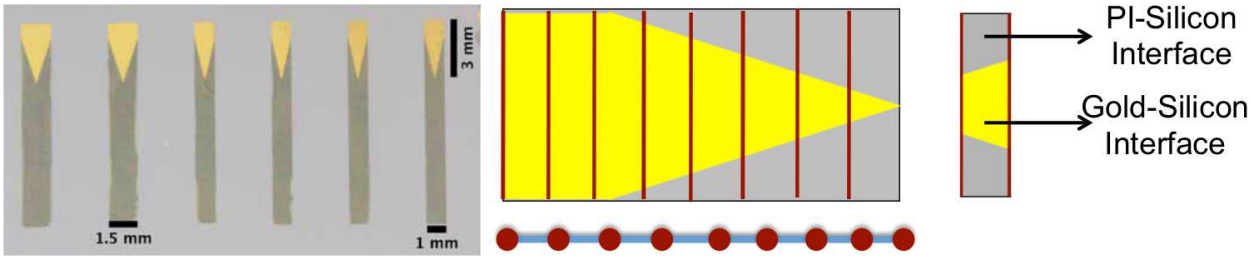

Figure 4.16 – (a) Image of PI specimens with triangular pre-crack. The polymer is clear and hence the triangular pre-crack region with the Au layer is clearly visible. In the image the pre-crack geometry spans 3 *mm* (*Image courtesy of Martha Grady*). (b) Modeling of triangular pre-crack: For each element in the triangular region, the respective area ratios are determined.

$$E(x) = E^{Weak}\hat{A}^{Weak} + E^{Strong}\hat{A}^{Strong}, \tag{4.19}$$

where the superscript *Weak* and *Strong* refers to the respective properties of the weak and strong interfaces while $\hat{A}$ represents the area ratio and $\hat{V}$ the volume ratio.

The pre-crack in all the cases considered here has a rectangular portion of 500 μm followed by a triangular portion that ensures the gradual transition to the stronger interface. The crack advance evolution for pre-cracks with triangular portions of varying lengths are compared in Figure 4.17. The longer the triangular region, the more gradual the transition of the interface toughness to that of the strong interface. As apparent in Figure 4.17, a longer triangular region yields a longer crack advance.

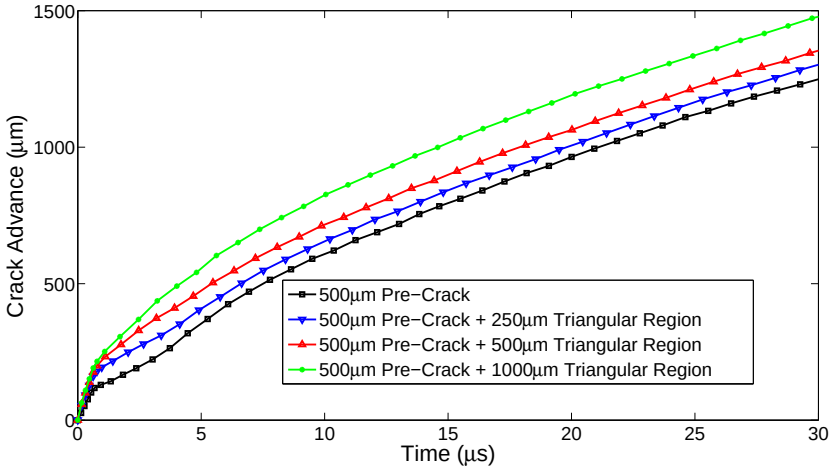

Figure 4.17 – Crack advance comparison for varying triangular portion lengths. The longer the triangular pre-crack, the longer the crack advance.

The evolution curves for the peak axial stress obtained for the different specimen configurations are compared in Figure 4.18. The triangular pre-crack portion provides a more gradual transition into the tougher interface and hence reduces the axial stresses induced in the film, from almost 150 *MPa* in the absence of a triangular region to approximately 120 *MPa* for the longer (1000 μm) transition region. A similar trend is observed for the evolution of peak bending stress: the longer the triangular region, the greater the reduction in the maximum bending stress (Figure 4.19). It is also observed that the time at which the maximum bending stress occurs slowly shifts with the change in the triangular portions length. The peak bending stresses are developed when the pre-crack has completely delaminated and when the film starts to curl up. Longer triangular portions result in complete pre-crack delamination being delayed and hence the maximum bending stress occurs at a later time during the delamination event.

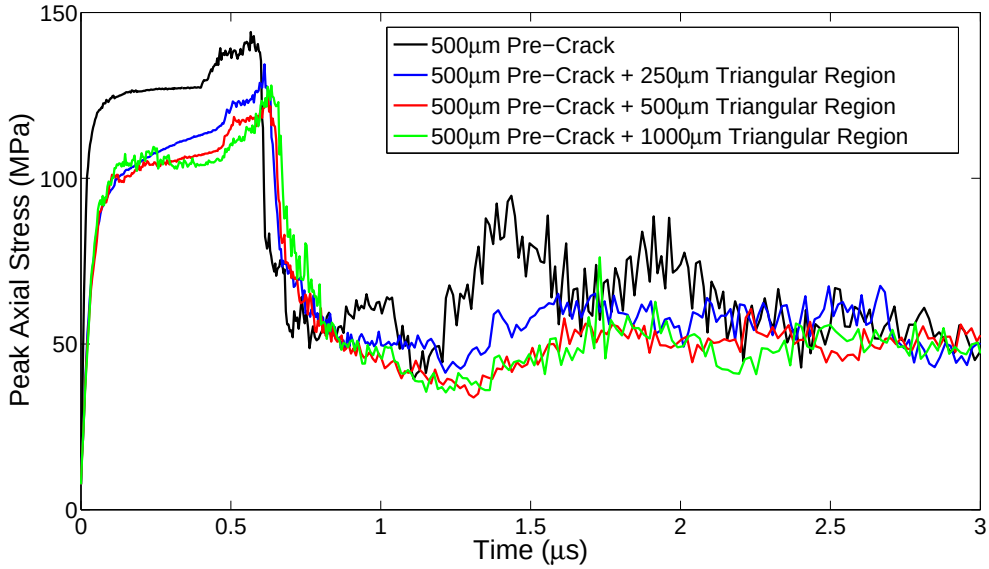

Figure 4.18 – Peak axial stress evolution for varying triangular portion lengths. For the pre-crack geometry with a 1000 μm triangular region, the maximum axial stress drops to about 120 *MPa* compared to a stress level of 150 *MPa* in the absence of a triangular portion.

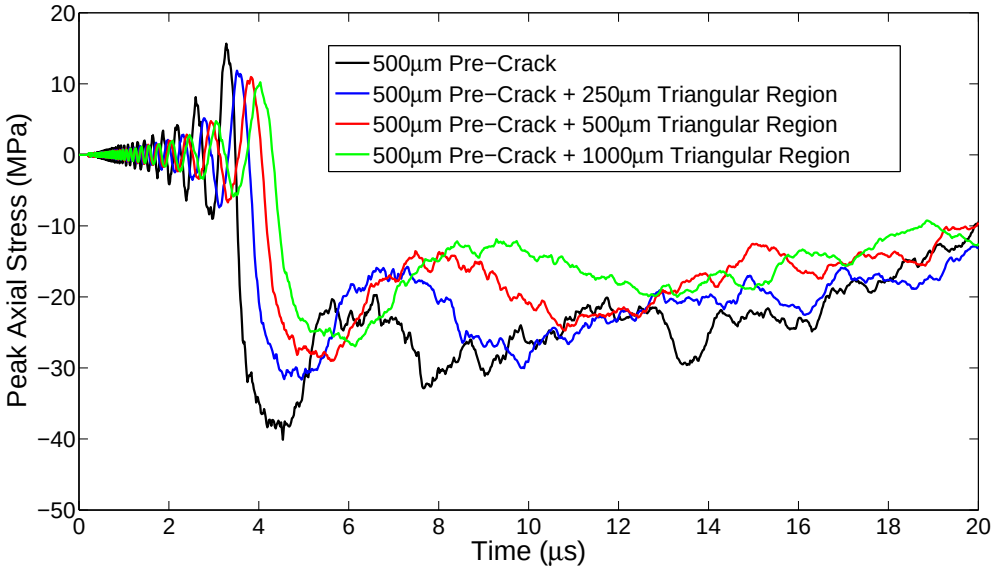

Figure 4.19 – Bending stress evolution for various triangular portion lengths showing the reduction of maximum bending stress with the increasing length of the triangular region.

4.4.2 Centered Pre-Crack Geometry

As indicated earlier, polymer films have very good adhesion properties and hence the crack advance is less compared to that of metallic films. The crack advance for Al films is in the range of 6-7 *mm* while for PI the crack advance is at most 2 *mm*. In general, the test samples are deposited on silicon substrates cut into 1 *in* squares with multiple test strips deposited on the substrate. The smaller crack advance observed in PI thus enables the accommodation of a larger number of strips. To increase the testing efficiency, modifications have thus been proposed to the pre-crack geometry, with the pre-crack placed at the center of PI film (Figure 4.20). When the centered pre-crack is hit with the laser-induced stress pulse, the film delaminates and the crack propagates on both sides of the centered pre-crack geometry. In effect, the centered geometry enables the testing of two samples at once, thereby improving testing efficiency as the setup time is reduced. The modification of the geometry alters the mechanics of the delamination as the film is more constrained: The original geometry referred to here as the "edge pre-crack" is not subjected to the same level of constraint as the centered pre-crack.

The centered pre-crack is modeled using symmetry boundary conditions as the additional constraint of the new geometry causes the film to bulge out instead of cleanly delaminating from the surface. The film behavior is symmetric about the centerline of the

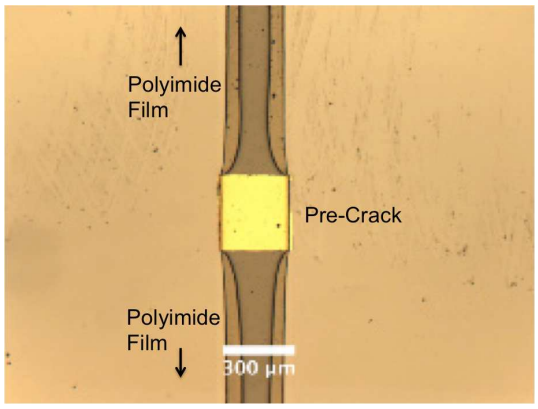

Figure 4.20 – Optical image of a centered pre-crack for PI film testing. The PI films run on either side of the rectangular gold pre-crack (*Image courtesy of Martha Grady*).

pre-crack and the symmetry boundary conditions are applied at this edge. The boundary conditions involve the enforcement of the zero horizontal displacement and zero slope conditions at the symmetric edge. Only vertical displacements are allowed at the symmetric edge and it is akin to placing the edge on vertical rollers as depicted in the schematic shown in Figure 4.21.

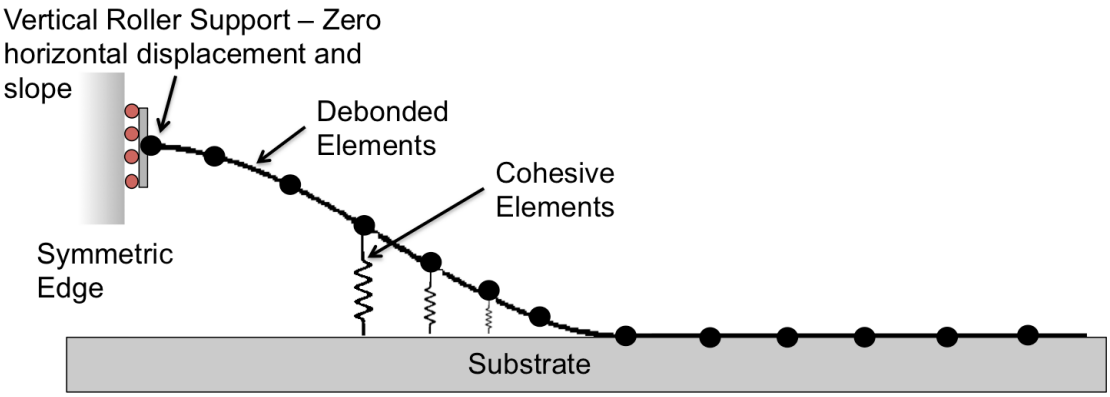

Figure 4.21 – Schematic of symmetric boundary condition used to simulate centered pre-crack, with the horizontal displacement and the slope at the symmetry edge set to zero.

The additional constraint results in the film bulging out and falling back down on the substrate. To avoid overlapping between the film and the substrate, the numerical model must be modified to include impenetrability constraints. In this work, this constraint is enforced directly through the cohesive formulation by defining a compressive traction-separation law for the cohesive elements. The compressive regime prevents the penetration of the substrate by providing a push-back force that is a strong function of the amount of penetration. The tangential tractions are governed by the same law as that

of the tensile loading case as described in Chapter 2. We adopt the following hyperbolic sine law for the normal traction law in the compression regime:

$$\hat{t}_n = e\hat{\sigma}_c exp\left(\frac{-\hat{\delta}_{max}}{\hat{\delta}_c}\right)\frac{1}{\alpha}sinh\left(\frac{\alpha\bar{\delta}_n}{\hat{\delta}_c}\right). \tag{4.20}$$

The traction-separation law is depicted in Figure 4.22 below for a range of normalized opening displacements. The special form of the compressive cohesive force ensures that the slope at the onset of the compressive regime matches that of the tensile regime at the origin, whether the tensile failure prior to unloading was complete (solid curve) or partial (dash-dotted curve). As apparent in the figure, which is obtained for a value of α of 5 the push-back force generated in the compressive regime increases sharply with the overlap displacement. For partial failure, i.e. when the δ_n is three times of δ_c, the unloading happens along the dash-dotted curve shown in Figure 4.22. When the δ_n is about ten times that of δ_c, the traction-separation curve becomes asymptotic to the x-axis and the element is considered to be completely failed. As apparent in the figure, even for the complete failure case, when the overlap displacement increases, the slope at the onset of the compressive regime is equal to that of the tensile regime.

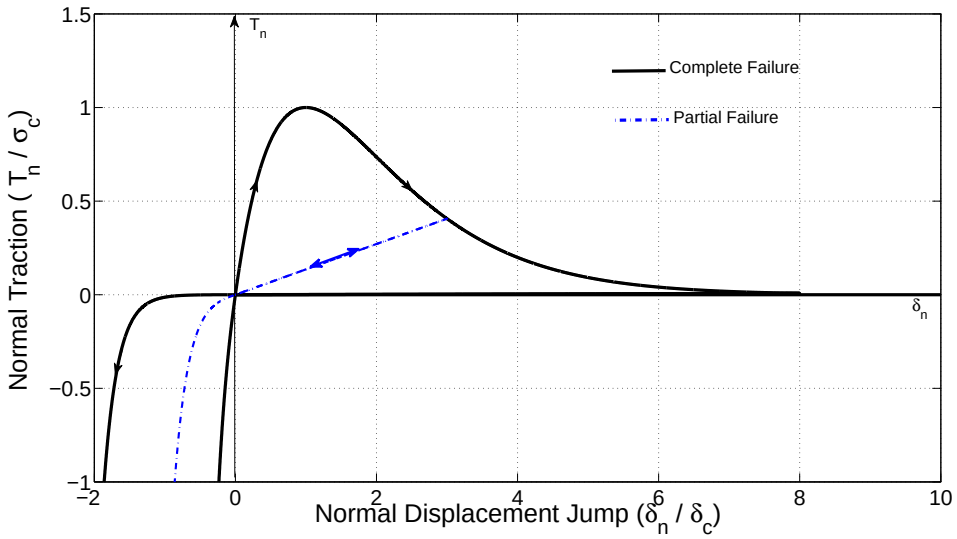

Figure 4.22 – Cohesive law with the impenetrability constraints, obtained for $\alpha = 5$. The solid and dashed curves respectively correspond to a complete and partial failure followed by unloading and compression, emphasizing the continuity of the cohesive traction slope at the onset of the compressive regime.

As mentioned before, the added constraint causes the film to bulge out instead of cleanly lifting off from the surface and curling as observed with the edge pre-crack case.

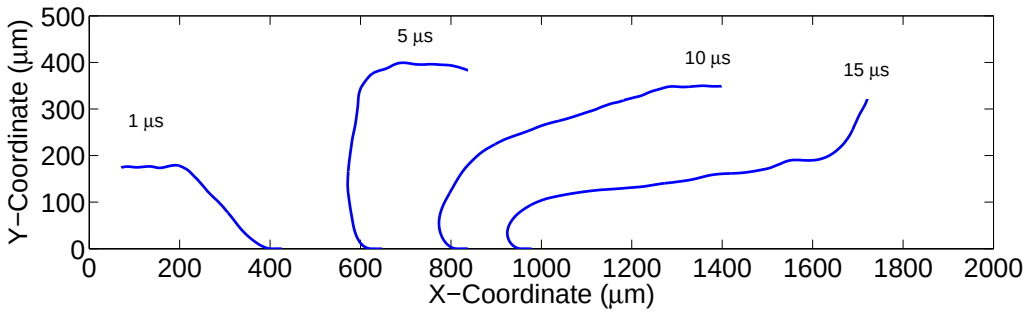

(a)

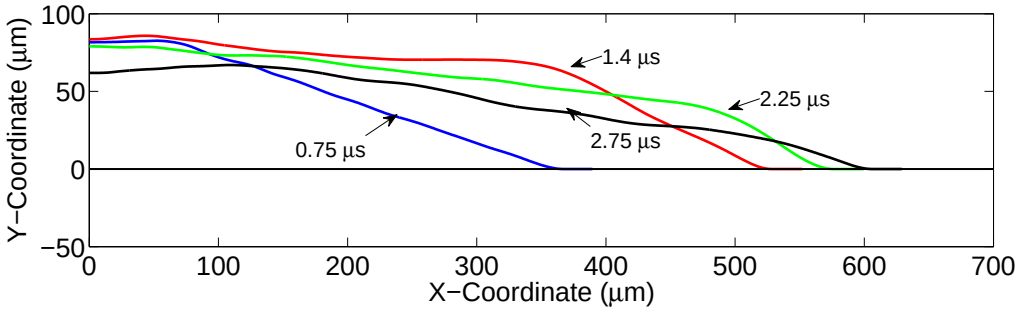

(b)

Figure 4.23 – Evolution of the shape of the delaminating film (a) for an edge pre-crack specimen, and (b) for a centered pre-crack specimen.

The delamination shapes of the film at various times are compared in Figure 4.23. The symmetric constraint restricts the film and prevents the film from curling up as seen in edge pre-crack cases. The crack advance obtained for both cases are compared in Figure 4.24. The centered pre-crack geometry results in crack propagation in both directions of the pre-crack and thus the effective pre-crack length for each crack propagation is half of the feature length as two tests are conducted with one laser pulse hit. It is observed that the crack advance obtained is about half that of the edge pre-crack case. On the other hand the crack tip velocity is much higher for the centered pre-crack due to the symmetric constraint channelling the energy into the fracture process at the interface. This is clearly observed in Figure 4.25, which presents a comparison of the mode mixity characterizing the failure processes. In the centered pre-crack case, the mode mixity drops to about 0.65 indicating that a significant shear loading component is generated due to the symmetric constraint.

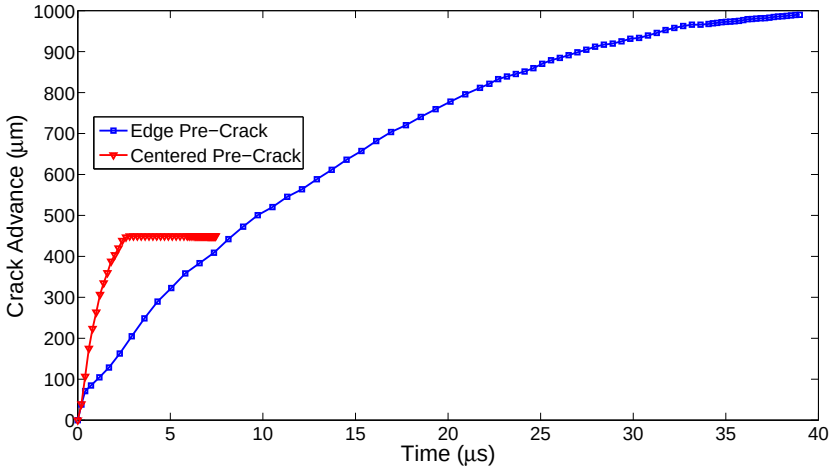

Figure 4.24 – Crack advance comparison between edge pre-crack and centered pre-crack geometries. The crack advance for symmetric constraint case is almost half of that the edge pre-crack case.

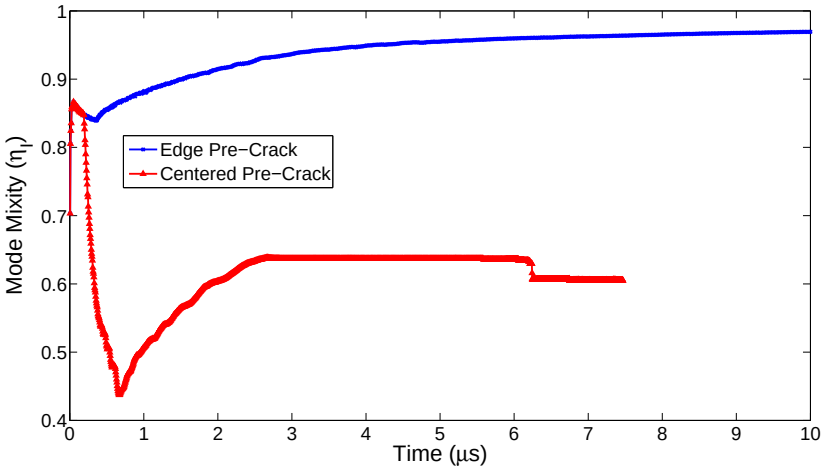

Figure 4.25 – Mode mixity comparison between the edge and centered pre-crack cases. The mode mixity level drops to 0.65 for centered pre-crack indicating a significant shear load component.

As observed in Figure 4.26, the axial stresses are significantly increased in the centered geometry due to the additional constraint. As apparent from the delamination shapes, there is a significant stretching of the film generated during the bulging event, thereby increasing the induced axial stresses by at least a factor of 2. As expected, little to no bending stress is observed in the centered geometry as the film is restrained from curling up as observed in Figure 4.27.

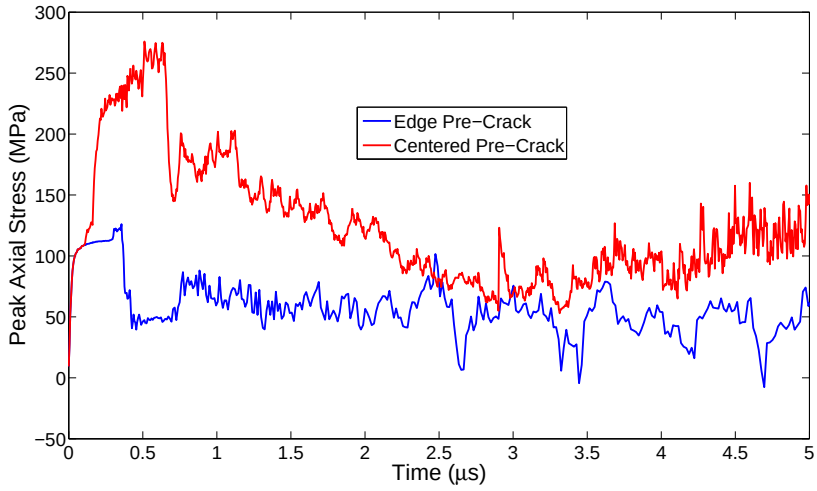

Figure 4.26 – Axial stress comparison between edge and centered cases, showing a substantial increment in stresses for the symmetric constraint case.

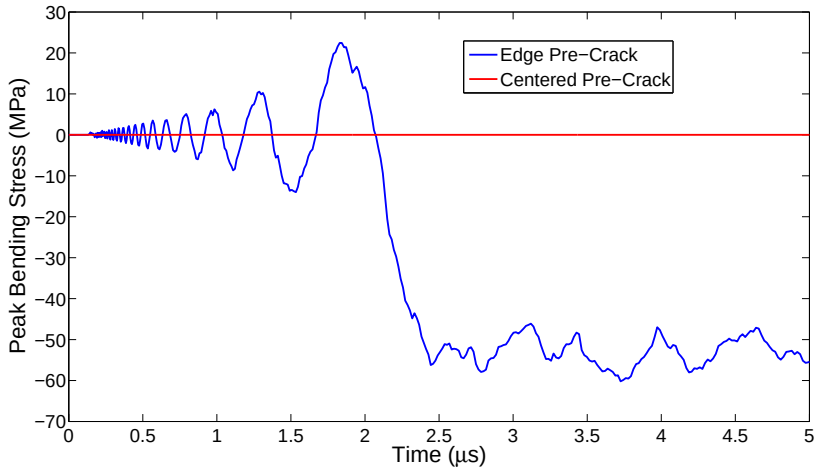

Figure 4.27 – Bending stress evolution in edge and centered pre-crack cases. The centered case has negligible bending stresses.

Chapter 5

Conclusions

The numerical models developed by Tran et al. [19] have been expanded to enable the study of film delamination under the influence of a variety of effects. The developed models have been used to evaluate the objectives stated in Chapter 1. The influence of residual stresses on film delamination has been extensively studied. A rational method was utilized wherein the arbitrary variation of residual stress across the film thickness was modeled as a series of polynomial distributions of increasing order. The loads generated by these polynomial distributions in terms of an equivalent axial force and bending moment have been determined, with the even polynomial distributions contributing only to the equivalent axial load and the odd distributions contributing to the equivalent bending moment. The tensile or compressive nature of the stress does not affect the crack evolution in the case of a mean residual stress loading. Mean residual stresses of the order of 300 *MPa* have been shown to increase the crack advance by about 2.5 *mm*. A residual stress magnitude of 300 *MPa* however falls on the higher side of measured experimental values: for lower residual stress values of the order of 100 *MPa* and less, the additional crack advance created by the presence of residual stresses is minimal. The study found that predictions based on simple strain energy release rate calculations match quite well with the dynamic simulations for the mean stress loading case. Also it was found that the mean stresses have a significant effect on the mode mixity of failure, reducing it to about 0.6, while the gradient stresses were found to have very little effect on the mode mixity of the delimitation process. Unlike mean stresses, the sign of the gradient stress distribution was found to have a significant impact on crack advance, as negative bending moments impeded crack growth and reduced the delamination length while positive moments aided in crack growth. The gradient stresses were found to cause the film to curl up and assume the delamination shape seen in testing.

Apart from the modeling of residual stress, several techniques to enable and improve the

efficiency of testing of polymer films were analyzed. The impact of adding an inertial layer to increase the trapped kinetic energy and hence crack advance was extensively studied. Among the candidate inertial layer materials, the most dense, silver, was determined to provide the most increase in trapped kinetic energy. The addition of a 1 μm-thick inertial layer of silver increased the crack advance by almost 350 μm compared to that obtained in the absence of inertial layer. It also reduced the peak axial stress by half to about 75 *MPa* from 150 *MPa*. The peak stresses developed during the initial laser loading was found to be strongly dependent on the interface toughness: the higher the interface toughness, the larger the peak stresses developed.

The use of a triangular pre-crack geometry to prevent the cohesive failure of the film was also studied. Triangular pre-cracks were found to be effective in reducing the peak stresses by about 30 *MPa*. This modified pre-crack geometry also led to an increase in the final crack advance, which was shown to varies linearly with the length of the triangular pre-crack region. Another proposed modification to the specimen geometry, based on the introduction of a centered pre-crack, was also investigated numerically by imposing a symmetry constraint to the motion o the edge of the film. We showed that the added constraint substantially changed the mode mixity of the failure process, inducing a significant shear loading component and yielding a mode mixity level of the order of 0.6. The centered pre-crack geometry also led to a significant increase in the peak stresses in the film: the peak axial stress induced in the film doubled up to about 280 *MPa* while the bending stresses were almost reduced to zero as the film was prevented from cleanly delaminating and curling up.

The numerical solver developed and modified in this work have thus provided a valuable tool to investigate, to first order, a variety of material- and geometry-related effects. To provide more information on the origin of the cohesive failure observed in the testing of polymer films, a more detailed study involving a more precise representation of the stress and strain states in the vicinity of the crack front immediately after the arrival of the laser-induced pulse is required. This more precise description combined with accurate models of the uniaxial and shear failure response of the film under high strain rates is necessary to address that issue.

Appendix A

Nonlinear Beam Element Formulation

The axial strain defined in Equation (2.4) is split into two separate components as

$$\epsilon_s = \frac{\partial u_0}{\partial x} + \frac{1}{2}\left(\frac{\partial w}{\partial x}\right)^2 \qquad and \tag{A.1}$$

$$\kappa = -\eta\frac{h}{2}\frac{\partial^2 w}{\partial x^2}. \tag{A.2}$$

The weak integral form of the dynamic equilibrium equation given by Equation (2.15) now becomes

$$\int_0^L \rho A \frac{\partial^2 \mathbf{u}}{\partial t^2}.\delta\mathbf{u}\, dx + \int_0^L \left(\varepsilon_s EA\delta\varepsilon_s + \kappa EI\delta\kappa\right)\, dx = \int_0^L \mathbf{T}.\delta\mathbf{\Delta}\, dx. \tag{A.3}$$

The last term of Equation (2.15) represents the external forces and such is determined by the loading conditions. Now using the shape functions for the element chosen the appropriate strain-displacement relationships are calculated. For the nonlinear beam elements these relationships are

$$\mathbf{B_u} = \frac{\partial \mathbf{u_0}}{\partial x} = \left\{\frac{-1}{L}, 0, 0, \frac{1}{L}, 0, 0\right\}, \tag{A.4}$$

$$\mathbf{B_w} = \frac{\partial \mathbf{w}}{\partial x} = \frac{1}{L}\{0, 6\xi\left(\xi-1\right), \left(1-\xi\right)\left(1-3\xi\right)L, 0, 6\xi\left(1-\xi\right), \xi\left(3\xi-3\right)L\}, \tag{A.5}$$

$$\mathbf{B_k} = \frac{\partial^2 \mathbf{w}}{\partial x^2} = \frac{1}{L^2}\{0, 6\left(1-2\xi\right), \left(4-6\xi\right)L, 0, 6\xi\left(1-2\xi\right), \left(2-6\xi\right)L\}. \tag{A.6}$$

The two strain components then become

$$\varepsilon_s = \mathbf{B_u u} + \frac{1}{2}\mathbf{u}^{\mathrm{T}}\mathbf{B}_{\mathbf{w}}^{\mathrm{T}}\mathbf{B_w u} \tag{A.7}$$

$$\kappa = \eta\frac{h}{2}\mathbf{B_k u}. \tag{A.8}$$

The first term of Equation (A.3) constitutes the mass matrix and the consistent mass matrix given below is used.

$$\mathbf{M} = \frac{\rho AL}{420}\begin{bmatrix} 140 & 0 & 0 & 70 & 0 & 0 \\ 0 & 156 & 22L & 0 & 54 & -13L \\ 0 & 22l & 4L^2 & 0 & 13L & -3L^2 \\ 70 & 0 & 0 & 140 & 0 & 0 \\ 0 & 54 & 13L & 0 & 156 & -22L \\ 0 & -13L & -3L^2 & 0 & -22L & 4L^2 \end{bmatrix}. \tag{A.9}$$

The second term of Equation (A.3) now becomes

$$\begin{aligned} &\int_0^L (\varepsilon_s EA\delta\varepsilon_s + \kappa EI\delta\kappa)\, dx \\ &\qquad = EA\int_0^L \delta\mathbf{u}^{\mathrm{T}}\left(\mathbf{B}_{\mathbf{u}}^{\mathrm{T}} + \mathbf{B}_{\mathbf{w}}^{\mathrm{T}}\mathbf{B_w u}\right)\left(\mathbf{B_u u} + \frac{1}{2}\mathbf{u}^{\mathrm{T}}\mathbf{B}_{\mathbf{w}}^{\mathrm{T}}\mathbf{B_w u}\right)dx \\ &\qquad + EI\int_0^L \delta\mathbf{u}^{\mathrm{T}}\mathbf{B}_{\mathbf{k}}^{\mathrm{T}}\mathbf{B_k u}dx. \end{aligned} \tag{A.10}$$

The internal force vector is determined by taking the first variation of Equation (A.10)

$$\begin{aligned} \mathbf{R_{in}} = EA&\int_0^L \left(\mathbf{B}_{\mathbf{u}}^{\mathrm{T}} + \mathbf{B}_{\mathbf{w}}^{\mathrm{T}}\mathbf{B_w u}\right)\left(\mathbf{B_u u} + \frac{1}{2}\mathbf{u}^{\mathrm{T}}\mathbf{B}_{\mathbf{w}}^{\mathrm{T}}\mathbf{B_w u}\right)dx \\ &+ EI\int_0^L \mathbf{B}_{\mathbf{k}}^{\mathrm{T}}\mathbf{B_k u}dx, \end{aligned} \tag{A.11}$$

and the above expression is expanded to obtain the final expression for the internal force vector as

$$\begin{aligned} \mathbf{R_{in}} = EA&\int_0^L \left(\mathbf{B}_{\mathbf{u}}^{\mathrm{T}}\mathbf{B_u u} + \frac{1}{2}\mathbf{B}_{\mathbf{u}}^{\mathrm{T}}\mathbf{u}^{\mathrm{T}}\mathbf{B}_{\mathbf{w}}^{\mathrm{T}}\mathbf{B_w u} + \mathbf{B}_{\mathbf{w}}^{\mathrm{T}}\mathbf{B_w u B_u u} + \frac{1}{2}\mathbf{B}_{\mathbf{w}}^{\mathrm{T}}\mathbf{B_w u u}^{\mathrm{T}}\mathbf{B}_{\mathbf{w}}^{\mathrm{T}}\mathbf{B_w u}\right)dx \\ &+ EI\int_0^L \left(\mathbf{B}_{\mathbf{k}}^{\mathrm{T}}\mathbf{B_k u}\right)dx. \end{aligned} \tag{A.12}$$

The tangent stiffness matrix is determined by taking the second variation of the above equation to get

$$\begin{aligned}\mathbf{K} = EA \int_0^L & \mathbf{B}_\mathbf{u}^\mathrm{T}\mathbf{B}_\mathbf{u}\Delta\mathbf{u} + \frac{1}{2}\left(\mathbf{B}_\mathbf{u}^\mathrm{T}\Delta\mathbf{u}^\mathrm{T}\mathbf{B}_\mathbf{w}^\mathrm{T}\mathbf{B}_\mathbf{w}\mathbf{u} + \mathbf{B}_\mathbf{u}^\mathrm{T}\mathbf{u}^\mathrm{T}\mathbf{B}_\mathbf{w}^\mathrm{T}\mathbf{B}_\mathbf{w}\Delta\mathbf{u}\right) \\ & + \left(\mathbf{B}_\mathbf{w}^\mathrm{T}\mathbf{B}_\mathbf{w}\Delta\mathbf{u}\mathbf{B}_\mathbf{u}\mathbf{u} + \mathbf{B}_\mathbf{w}^\mathrm{T}\mathbf{B}_\mathbf{w}\mathbf{u}\mathbf{B}_\mathbf{u}\Delta\mathbf{u}\right) \\ & + \frac{1}{2}\left(\mathbf{B}_\mathbf{w}^\mathrm{T}\mathbf{B}_\mathbf{w}\Delta\mathbf{u}\mathbf{u}^\mathrm{T}\mathbf{B}_\mathbf{w}^\mathrm{T}\mathbf{B}_\mathbf{w}\mathbf{u} + \mathbf{B}_\mathbf{w}^\mathrm{T}\mathbf{B}_\mathbf{w}\mathbf{u}\Delta\mathbf{u}^\mathrm{T}\mathbf{B}_\mathbf{w}^\mathrm{T}\mathbf{B}_\mathbf{w}\mathbf{u} + \mathbf{B}_\mathbf{w}^\mathrm{T}\mathbf{B}_\mathbf{w}\mathbf{u}\mathbf{u}^\mathrm{T}\mathbf{B}_\mathbf{w}^\mathrm{T}\mathbf{B}_\mathbf{w}\Delta\mathbf{u}\right) dx \\ & + EI \int_0^L \left(\mathbf{B}_\mathbf{k}^\mathrm{T}\mathbf{B}_\mathbf{k}\Delta\mathbf{u}\right) dx.\end{aligned} \tag{A.13}$$

The tangent stiffness matrix is then identified as

$$\begin{aligned}\mathbf{K} = EA \int_0^L & \left(\mathbf{B}_\mathbf{u}^\mathrm{T}\mathbf{B}_\mathbf{u} + \mathbf{B}_\mathbf{u}^\mathrm{T}\mathbf{u}^\mathrm{T}\mathbf{B}_\mathbf{w}^\mathrm{T}\mathbf{B}_\mathbf{w} + \mathbf{B}_\mathbf{w}^\mathrm{T}\mathbf{B}_\mathbf{u}\mathbf{u}\mathbf{B}_\mathbf{w} + \mathbf{B}_\mathbf{w}^\mathrm{T}\mathbf{B}_\mathbf{w}\mathbf{u}\mathbf{B}_\mathbf{u} + \frac{3}{2}\mathbf{B}_\mathbf{w}^\mathrm{T}\mathbf{B}_\mathbf{w}\mathbf{u}\mathbf{u}^\mathrm{T}\mathbf{B}_\mathbf{w}^\mathrm{T}\mathbf{B}_\mathbf{w}\right) dx \\ & + EI \int_0^L \mathbf{B}_\mathbf{k}^\mathrm{T}\mathbf{B}_\mathbf{k} dx.\end{aligned} \tag{A.14}$$

Appendix B

Residual Stress Formulation

The new definition of stress that includes the residual stress is used to obtain the formulation. The total stress component is broken down into the internal stress component (σ_{in}), axial stress component due to residual stresses (σ_{Rax}), and the bending stress component due to residual stress (σ_{Rmom}). Assuming a linear material model this definition is used in Equation (A.10) to obtain the following

$$
\begin{aligned}
L\int_0^1 &\left(\varepsilon_s EA\delta\varepsilon_s + \kappa EI\delta\kappa + \varepsilon_{Rax}EA\delta\varepsilon_s + \kappa_{Rmom}EI\delta\kappa\right), d\varepsilon \\
&= LEA\int_0^1 \delta\mathbf{u}^{\mathbf{T}}\left(\mathbf{B_u^T} + \mathbf{B_w^T B_w u}\right)\left(\mathbf{B_u u} + \frac{1}{2}\mathbf{u}^{\mathbf{T}}\mathbf{B_w^T B_w u}\right)d\varepsilon \\
&+ LEI\int_0^1 \delta\mathbf{u}^{\mathbf{T}}\mathbf{B_k^T B_k u}d\varepsilon \\
&+ LEA\int_0^1 \delta\mathbf{u}^{\mathbf{T}}\left(\mathbf{B_u^T} + \mathbf{B_w^T B_w u}\right)\varepsilon_{Rax}d\varepsilon \\
&+ LEI\int_0^1 \delta\mathbf{u}^{\mathbf{T}}\mathbf{B_k^T}\varepsilon_{Rmom}d\varepsilon.
\end{aligned}
\tag{B.1}
$$

We know that σ_{Rax} results only in the axial extension of the beam as it generates only a net axial load. For this reason the only the appropriate strain components are used. Similarly the σ_{Rmom} is known only to induce a net moment and hence only the appropriate bending strain terms are used. The first variation of the above equation then yields the internal

force vector as

$$\begin{aligned}\mathbf{R_{in}} = LEA \int_0^1 \left(\mathbf{B_u^T} + \mathbf{B_w^T B_w u}\right)\left(\mathbf{B_u u} + \frac{1}{2}\mathbf{u}^T\mathbf{B_w^T B_w u}\right) d\varepsilon \\ + LEI \int_0^1 \mathbf{B_k^T B_k u} d\varepsilon \\ + LEA \int_0^1 \left(\mathbf{B_u^T} + \mathbf{B_w^T B_w u}\right) \varepsilon_{Rax} d\varepsilon \\ + LEI \int_0^1 \mathbf{B_k^T} \varepsilon_{Rmom} d\varepsilon.\end{aligned} \tag{B.2}$$

The tangent stiffness matrix is obtained by taking the second variational derivative of the weak integral form. The second variational derivative would be of the form

$$\begin{aligned}\mathbf{K} = LEA \int_0^1 \mathbf{B_u^T B_u}\Delta\mathbf{u} + \frac{1}{2}\left(\mathbf{B_u^T}\Delta\mathbf{u}^T\mathbf{B_w^T B_w u} + \mathbf{B_u^T u}^T\mathbf{B_w^T B_w}\Delta\mathbf{u}\right) \\ + \left(\mathbf{B_w^T B_w}\Delta\mathbf{u B_u u} + \mathbf{B_w^T B_w u B_u}\Delta\mathbf{u}\right) \\ + \frac{1}{2}\left(\mathbf{B_w^T B_w}\Delta\mathbf{u u}^T\mathbf{B_w^T B_w u} + \mathbf{B_w^T B_w u}\Delta\mathbf{u}^T\mathbf{B_w^T B_w u} + \mathbf{B_w^T B_w u u}^T\mathbf{B_w^T B_w}\Delta\mathbf{u}\right) d\varepsilon \\ + LEI \int_0^1 \left(\mathbf{B_k^T B_k}\Delta\mathbf{u}\right) d\varepsilon \\ + LEA \int_0^1 \left(\mathbf{B_w^T B_w}\Delta\mathbf{u}\right) \varepsilon_{Rax} d\varepsilon.\end{aligned} \tag{B.3}$$

The tangent stiffness matrix is then identified as

$$\begin{aligned}\mathbf{K} = LEA \int_0^1 \left(\mathbf{B_u^T B_u} + \mathbf{B_u^T u}^T\mathbf{B_w^T B_w} + \mathbf{B_w^T B_u u B_w} + \mathbf{B_w^T B_w u B_u} + \frac{3}{2}\mathbf{B_w^T B_w u u}^T\mathbf{B_w^T B_w}\right) d\varepsilon \\ + LEI \int_0^1 \mathbf{B_k^T B_k} d\varepsilon \\ + LEA \int_0^1 \left(\mathbf{B_w^T B_w}\right) \varepsilon_{Rax} d\varepsilon.\end{aligned} \tag{B.4}$$

References

[1] A. G. Evans and J. Hutchinson, "The thermomechanical integrity of thin films and multi-layers," *Acta Metallurgica et Materialia*, vol. 43, pp. 2507–2530, 1995.

[2] D. He, D. Zhang, T. Chiang, R. Lucero, R. Stage, and V. Atluri, "Comparison of thin film cracking and delamination for aluminum and copper silicon interconnects with organic packaging," *In Proceedings: IEEE Electronic Components and Technology Conference*, pp. 349–355, 2005.

[3] G. Q. Zhang, X. J. Van Driel, and W. D. Fan, *Mehanics of Microelectronics - Solid Mechanics and its Applications*. Springer, 2006.

[4] S. Kandula, *Delamination of thin film patterns using laser-induced stress wave*. PhD thesis, University of Illinois, 2008.

[5] S. Kandula, P. Tran, P. H. Geubelle, and N. R. Sottos, "Dynamic delamination of patterned thin films," *Applied Physics Letters*, vol. 93, pp. 261902–1, 2008.

[6] K. S. Kim and J. Kim, "Elasto-plastic analysis of the peel test for thin film adhesion," *Journal of Engineering Materials and Technology - Transaction ASME*, vol. 110(3), pp. 266–273, 1988.

[7] Y. Z. Chu, H. S. Jeong, R. C. White, and C. J. Durning, "Characterization of adhesion in thin-film materials by the blister test," *MRS Symposium Proceedings*, vol. 276, pp. 209–220, 1992.

[8] Z. Gan, S. G. Mhaisalkar, Z. Chen, and K. Zhang, S.and Prasad, "Study of interfacial adhesion energy of multilayered ulsi thin film structure using four-point bending test," *Surface and Coating Technology*, vol. 198, pp. 85–89, 2005.

[9] M. D. Kriese, W. W. Gerberich, and N. Moody, "Quantitative adhesion measures of multilayer films: Part i. indentation mechanics," *Journal of Materials Research*, vol. 14(7), pp. 3007–3018, 1999.

[10] A. Evans, J. W. Hutchinson, and Y. Wei, "Interface adhesion: Effects of plasticity and segregation," *Acta Materialia*, vol. 47, pp. 4093–4113, 1999.

[11] P. Tran, *Dynamic Delamination of Patterned Thin Films*. PhD thesis, University of Illinois, 2010.

[12] V. Gupta, A. S. Argon, J. A. Cornie, and D. M. Parks, "Measurement of interface strength by laser pulse-induced spallation," *Material Science and Engineering.*, vol. 125, pp. 105–117, 1990.

[13] V. Gupta, A. S. Argon, D. M. Parks, and J. A. Cornie, "Measurement of interface strength by a laser spallation technique," *Journal of the Mechanics and Physics of Solids*, vol. 40, pp. 141–180, 1992.

[14] J. Wang, *Thin film adhesion measurement by laser induced stress waves*. PhD thesis, University of Illinois, 2002.

[15] J. L. Vossen, "Measurements of film-substrate bond strength by laser spallation. adhesion measurement of thin films, thick films and bulk coatings, ASTM STP 640," *American Society for Testing and Materials*, vol. 640, pp. 122–123, 1978.

[16] J. Wang, R. L. Weaver, and N. R. Sottos, "A parametric study of laser induced thin film spallation," *Experimental Mechanics*, vol. 42, pp. 74–83, 2002.

[17] J. Wang, N. R. Sottos, and R. L. Weaver, "Mixed-mode failure of thin films using laser generated shear waves," *Experimental Mechanics*, vol. 43, pp. 323–330, 2003.

[18] R. Kitey, P. Geubelle, and N. Sottos, "Mixed-mode interfacial adhesive strength of a thin film on an anisotropic substrate," *Journal of the Mechanics and Physics of Solids*, vol. 57, pp. 51–64, 2009.

[19] P. Tran, S. Kandula, P. Geubelle, and N. Sottos, "Dynamic delamination of patterned thin films a numerical study," *International Journal of Fracture*, vol. 75, pp. 4217–4233, 2009.

[20] Z. Suo and J. W. Hutchinson, "Interface crack between two elastic layers," *International Journal of Fracture*, vol. 43, pp. 1–18, 1990.

[21] J. W. Hutchinson and Z. Suo, "Mixed mode cracking in layered materials," *Advances in Applied Mechanics*, vol. 29, pp. 63–191, 1992.

[22] M. Hu, M. Thouless, and A. Evans, "The decohesion of thin films from brittle substrates," *Acta Metallurgica*, vol. 36, pp. 1301–1307, 1988.

[23] M. Thouless and H. Jensen, "The effect of residual stresses on adhesion measurements," *Jornal of Micromechanics and Microengineering*, vol. 8, pp. 579–586, 1994.

[24] D. Dugdale, "Yielding of steel sheets containing slits," *Journal of Mechanics and Physics of Solids*, vol. 8, pp. 100–104, 1960.

[25] G. Barrenblatt, "The mathematical theory ofequilibrium of cracks in brittle fracture," *Advances in Applied Mechanics*, vol. 7, pp. 55–129, 1962.

[26] J. R. Rice, *Mathematical analysis in the mechanics of fracture - Fracture, Liebowitz (ed.)*. Academic Press, 1968.

[27] N. Jansson, Y. Leterrier, and J. Manson, "Modeling of multiple cracking and decohesion of a thin film on a polymer substrate," *Engineering Fracutre Mehanics*, vol. 73, pp. 2614–26, 2006.

[28] T. Shield and K. Kim, "Beam theory models for thin film segments cohesively bonded to an elastic half space," *International Journal of Solids and Structures*, vol. 29(9), pp. 1085–103, 1992.

[29] A. Fedorov, R. Tijum, W. Vellinga, and J. De Hosson, "Work of adhesion in laser-induced delamination along polymer-metal interfaces," *Journal of Applied Physics*, vol. 101(4), 2007.

[30] W. Li and T. Siegmund, "An analysis of the indentation test to determine the interface toughness in a weakly bonded thin film coating-substrate system.," *Acta Materialia*, vol. 52, pp. 2989–99, 2004.

[31] Y. Liang, X. Bi, and J. Wang, "Numerical simulation of laser-induced thin film delamination," *Thin Solid Films*, vol. 516, pp. 971–981, 2008.

[32] P. Tran, S. Kandula, P. Geubelle, and N. Sottos, "Hybrid spectral/finite element analysis of dynamic delamination of patterned thin films," *Engineering Fracture Mechanics*, vol. 75, pp. 4217–4233, 2008.

[33] P. Geubelle and J. Baylor, "Impact-induced delamination of composites: a 2d simulation," *Composites Part B: Engineering*, vol. 29B, pp. 589–602, 1998.

[34] Y. Zhang and Y. Zhao, "An effective method of determining the residual stress gradients in a micro-cantilever," *Microsystem Technologies*, vol. 12, pp. 357–364, 2006.

[35] J. Simo and L. Vu-Quoc, "The role of non-linear theory in transient dynamic analysis of flexible structures," *Journal of Sound and Vibration*, vol. 119(3), pp. 487–508, 1987.

[36] M. Kulkarni, P. Geubelle, and K. Matous, "Multi-scale modeling of heterogenous adhesives: Effect of particle decohesion," *Mechanics of Materials*, vol. 41, pp. 573–583, 2008.

[37] A. Pandolfi and M. Ortiz, "Finite-deformation irreversible cohesive elements for three-dimensional crack-propagation analysis," *International Journal for Numerical Methods in Engineering*, vol. 55, pp. 1285–1322, 2002.

[38] M. Crisfield and G. Cole, "Co-rotational beam elements for two- and three- dimensional non-linear analysis," *Proceedings of the IUTAM/IACM Symposium on Discretization Methods in Structural Mechanics*, vol. 4, pp. 115–124, 1989.

[39] T. J. R. Hughes, *Linear Static and Dynamic Finite Element Analysis*. Prentice-Hall Inc, 1987.

[40] L. B. Freund and S. Suresh, *Thin Film Materials: Stress, defect formation and surface evolution*. Cambridge University Press, 2003.

[41] A. Bagchi, G. Lucas, Z. Suo, and A. Evans, "A new procedure for measuring the decohesion energy for thin ductile films on substrates," *Journal of Materials Research*, vol. 9, pp. 1734–1741, 1994.

[42] W. Fang and J. Wickert, "Determining mean and gradient residual stresses in thin films using micromachined cantilevers.," *Journal of Micromechanics and Microengineering*, vol. 6, pp. 301–309, 1996.

[43] K. F. Graff, *Wave Propagation in Elastic Solids*. Clarendon Press, 1975.

[44] X. Xue, K. Kozaczek, D. Kurtz, and S. Kurtz, "Estimating residual stress tensor in aluminum and copper thin films and interconnects," *Advances in X-ray Analysis*, vol. 42, pp. 612–622, 2000.

[45] Y. Min and Y. Kim, "In situ measurements of residual stress in micromachined thin films using a specimen with composite-layered cantilevers," *Journal of Micromechanics and Microengineering*, vol. 10, pp. 314–321, 2000.

[46] M. Drory, M. Thouless, and A. Evans, "On the decohesion of residually-stresses thin films," *Acta Mettalurgica*, vol. 36, pp. 2019–2028, 1988.

[47] G. Maier, "Polymers for microelectronics," *Materials Today*, vol. 4, pp. 22–33, 2001.

[48] M. Angelopoulos, "Conducting polymers in microelectronics," *IBM Journal of Research and Development*, vol. 45, pp. 57–75, 2001.

[49] M. Piggott and C. .P.S., "The glass fibre-polymer interface: Ii - work of fracture and shear stresses," *Composites Science and Technology*, vol. 22, pp. 107–119, 1985.

[50] S. Paul and C. .J.A., "Apparent modulus of a composite beam," *University of Cambridge Report*.

[51] K. Gramoll, *Mechanics*. Oklahoma University, 2000.

[52] J. Zheng and K. Sitaraman, "Fixtureless superlayer-driven delamination test for nanoscale thin-film interfaces," *Thin Solid Films*, vol. 515, pp. 4709–4716, 2007.

Author's Biography

Premsainath Coimbatore Selvarasu was born on June 25th, 1985 in the southern Indian city of Coimbatore. He obtained his Bachelors degree in Mechanical Engineering from *PSG College of Technology* an autonomous institution affiliated to Anna University in June, 2006. Soon after graduation he worked as an engineer for *GE Energy*, at the John F Welch Technology Center in Bangalore, India. Premsainath was involved in the mechanical design of gas and wind turbines. During his time at GE Energy, Premsainath was selected for the prestigious *Edison Engineering Development Program* which he was a part of till January 2009.

In January 2009, Premsainath began his graduate studies in the Aerospace Engineering Department at the University of Illinois at Urbana-Champaign. Under the guidance of Prof. Philippe H. Geubelle, Premsainath joined the Thin films research group at the University of Illinois, where his work focused on developing numerical models to simulate laser-induced delamination testing, a novel testing technique used to measure interface properties of thin films.